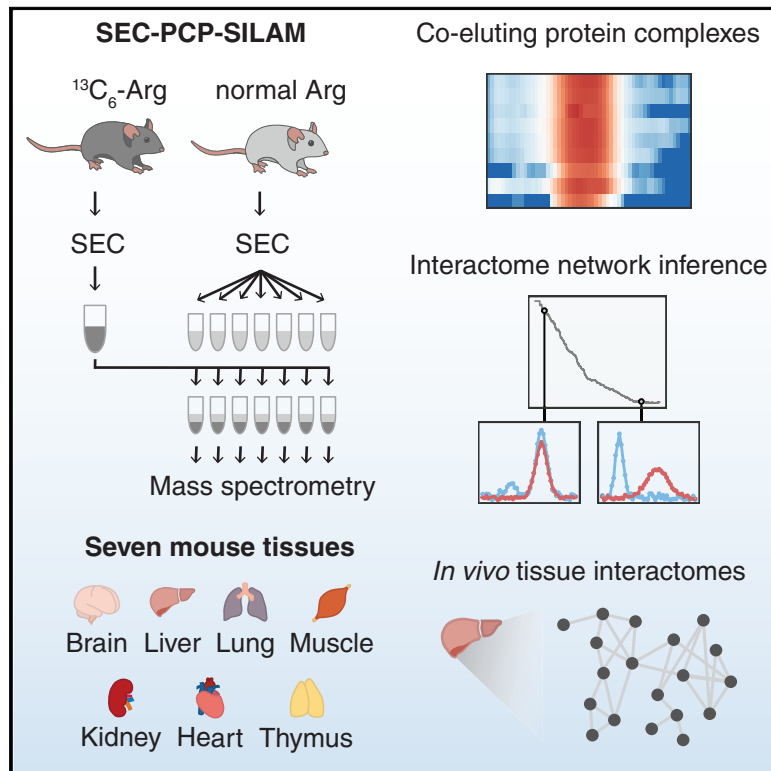


# An atlas of protein-protein interactions across mouse tissues

## Graphical abstract



## Authors

Michael A. Skinnider, Nichollas E. Scott, Anna Prudova, ..., David Rattray, Jörg Gsponer, Leonard J. Foster

## Correspondence

gsponer@msl.ubc.ca (J.G.),  
foster@msl.ubc.ca (L.J.F.)

## In brief

Systematic *in vivo* mapping of protein-protein interactions in seven mouse tissues provides insights into tissue-specific interaction rewiring and its role in disease.

## Highlights

- PCP-SILAM enables *in vivo* interactome mapping of seven mouse tissues
- A high-quality map more than doubles the size of the known mouse interactome
- Rewiring of protein interactions across tissues is tightly regulated
- Proteins implicated in tissue-specific diseases form tissue-specific subnetworks

Resource

# An atlas of protein-protein interactions across mouse tissues

Michael A. Skinnider,<sup>1,4</sup> Nichollas E. Scott,<sup>1,2,4</sup> Anna Prudova,<sup>1</sup> Craig H. Kerr,<sup>1,3</sup> Nikolay Stoyanov,<sup>1</sup> R. Greg Stacey,<sup>1</sup> Queenie W.T. Chan,<sup>1</sup> David Rattray,<sup>1,3</sup> Jörg Gsponer,<sup>1,3,\*</sup> and Leonard J. Foster<sup>1,3,5,\*</sup>

<sup>1</sup>Michael Smith Laboratories, University of British Columbia, Vancouver, BC V6T 1Z4, Canada

<sup>2</sup>Peter Doherty Institute, Department of Microbiology and Immunology, The University of Melbourne, Melbourne, VIC 3000, Australia

<sup>3</sup>Department of Biochemistry & Molecular Biology, University of British Columbia, Vancouver, BC V6T 1Z3, Canada

<sup>4</sup>These authors contributed equally

<sup>5</sup>Lead contact

\*Correspondence: [gsponer@msl.ubc.ca](mailto:gsponer@msl.ubc.ca) (J.G.), [foster@msl.ubc.ca](mailto:foster@msl.ubc.ca) (L.J.F.)

<https://doi.org/10.1016/j.cell.2021.06.003>

## SUMMARY

Cellular processes arise from the dynamic organization of proteins in networks of physical interactions. Mapping the interactome has therefore been a central objective of high-throughput biology. However, the dynamics of protein interactions across physiological contexts remain poorly understood. Here, we develop a quantitative proteomic approach combining protein correlation profiling with stable isotope labeling of mammals (PCP-SILAM) to map the interactomes of seven mouse tissues. The resulting maps provide a proteome-scale survey of interactome rewiring across mammalian tissues, revealing more than 125,000 unique interactions at a quality comparable to the highest-quality human screens. We identify systematic suppression of cross-talk between the evolutionarily ancient housekeeping interactome and younger, tissue-specific modules. Rewired proteins are tightly regulated by multiple cellular mechanisms and are implicated in disease. Our study opens up new avenues to uncover regulatory mechanisms that shape *in vivo* interactome responses to physiological and pathophysiological stimuli in mammalian systems.

## INTRODUCTION

Cellular functions are mediated by the dynamic association of individual proteins into complexes, signaling pathways, and other macromolecular assemblies. The biological functions of many proteins depend on specific physical interactions with other proteins, and disruption of these interactions can result in disease (Sahni et al., 2015; Wang et al., 2012). Defining the complete map of functional protein-protein interactions in a given organism (the interactome) has therefore been a long-standing goal of the post-genomic era, with a view to better understanding protein function, cellular processes, and ultimately the relationship between genotype and phenotype (Vidal et al., 2011). To this end, high-throughput methods have been developed to map interactomes at the proteome scale, including yeast two-hybrid (Y2H), affinity purification-mass spectrometry (AP-MS), protein complementation assay (PCA), and protein correlation profiling (PCP). These methods have been applied successfully to generate high-quality maps of the interactomes of humans (Hein et al., 2015; Huttlin et al., 2015, 2017; Luck et al., 2020; Rolland et al., 2014) and other metazoans (Guruharsha et al., 2011; Simonis et al., 2009).

Widely used methods for mammalian interactome mapping rely on heterologous expression or genetically manipulated cell lines, and, as a consequence, existing interactome maps provide

limited insight into which interactions occur in specific cell types or tissues, or under pathophysiologically relevant conditions (Snider et al., 2015). Targeted interactome mapping in tissue- or cell-type-specific contexts has revealed rewiring of protein interactions in select human diseases (Pankow et al., 2015; Shirasaki et al., 2012), yet fundamental questions regarding the organization of the interactome across mammalian tissues remain unanswered. Whereas large-scale efforts to profile the transcriptome, proteome, and epigenome of human tissues have been undertaken (Melé et al., 2015; Kundaje et al., 2015; Uhlen et al., 2015), a comparable resource at the interactome level is lacking.

We previously developed a high-throughput method for interactome mapping by combining size exclusion chromatography (SEC) with protein correlation profiling-stable isotope labeling by amino acids in cell culture (PCP-SILAC) (Kristensen et al., 2012). Here, we couple PCP with stable isotope labeling of mammals (SILAM) (Krüger et al., 2008; McClatchy et al., 2007) to map the interactomes of seven mouse tissues. This resource provides a global view of protein-protein interactions in a mammalian tissue-specific context. Our study additionally provides a systematic interactome map in mouse that more than doubles the size of the known mouse interactome. The resulting *in vivo* interactome maps uncover widespread rewiring of protein interactions across physiological contexts.

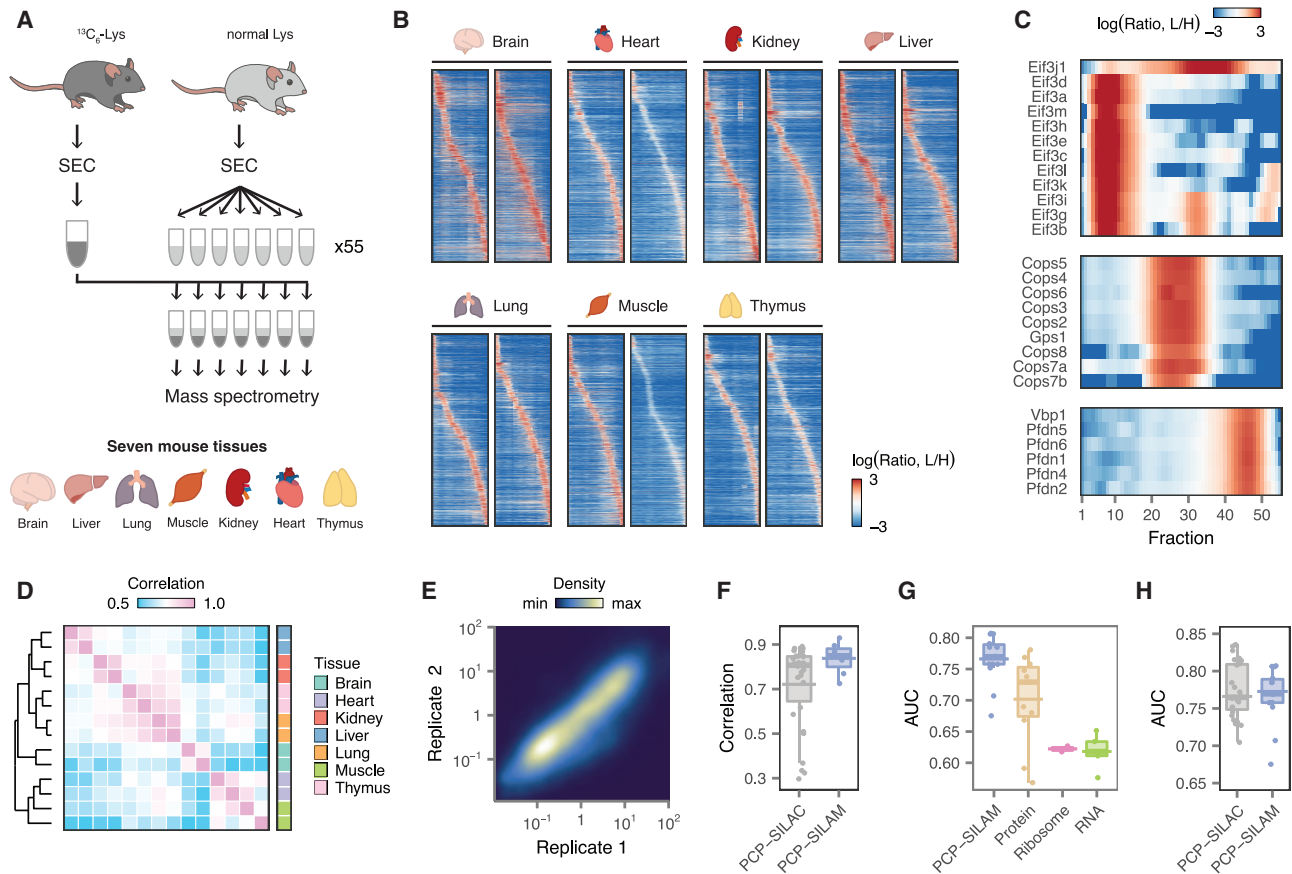


**Figure 1. Quantitative interactome profiles of seven mouse tissues with PCP-SILAM**

(A) PCP-SILAM workflow for interactome mapping in mouse tissues.

(B) Global visualization of protein elution profiles across 770 SEC fractions spanning seven mouse tissues. Elution profiles are arranged separately within each replicate by the fraction of maximum abundance.

(C) Enlarged elution profiles of representative protein complexes (top, eIF3 complex; middle, COP9 signalosome; bottom, prefoldin complex).

(D) Hierarchical clustering of PCP-SILAM replicates.

(E) Reproducibility of PCP-SILAM protein quantification.

(F) Rank correlations between biological replicates in PCP-SILAM and in published PCP-SILAC data. Horizontal lines show the mean correlation. Box plots show the median (horizontal line), interquartile range (hinges), and smallest and largest values no more than 1.5 times the interquartile range (whiskers) throughout.

(G) Recovery of known protein complexes by patterns of co-abundance in PCP-SILAM data, as compared to large-scale proteomics, transcriptomics, and ribosome profiling datasets. Horizontal line shows the mean AUC.

(H) Recovery of known protein complexes in PCP-SILAM and published PCP-SILAC data.

See also [Figure S1](#).

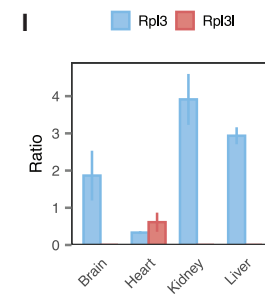
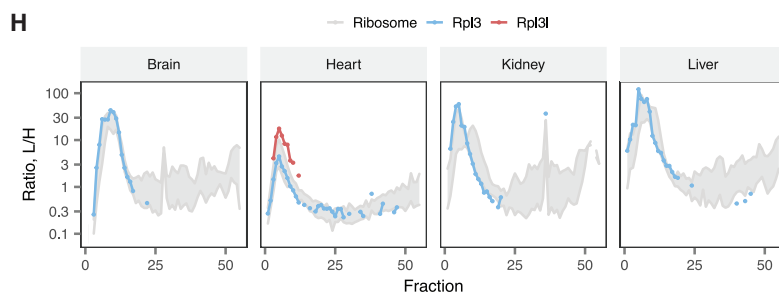
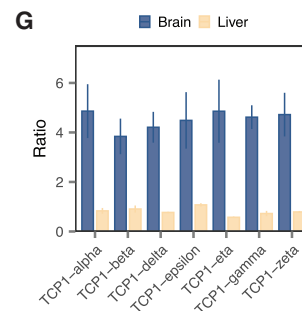
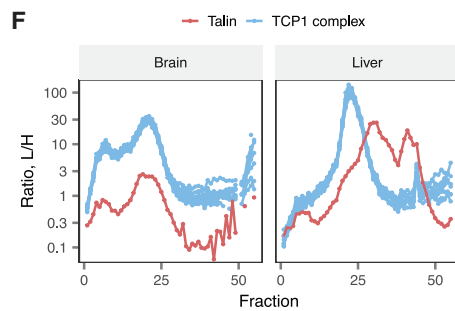
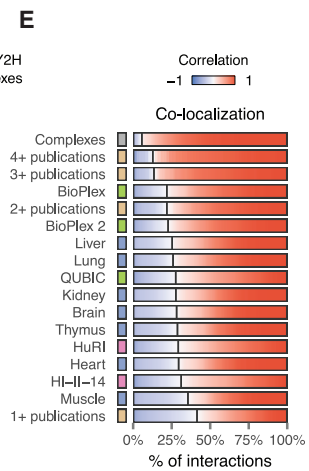
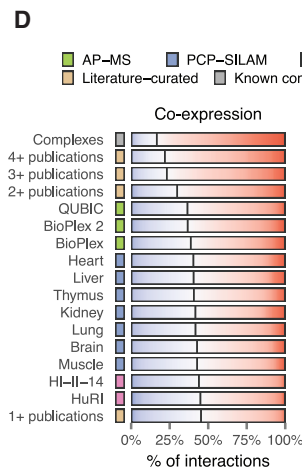
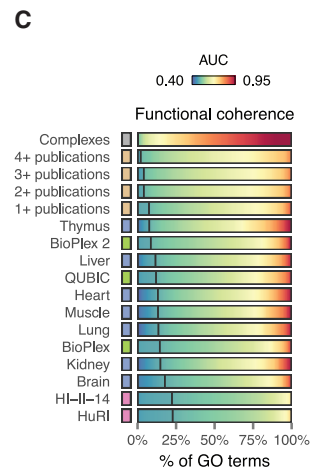
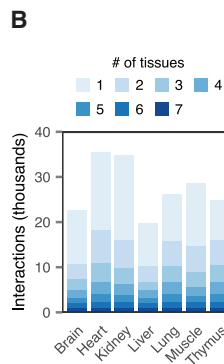
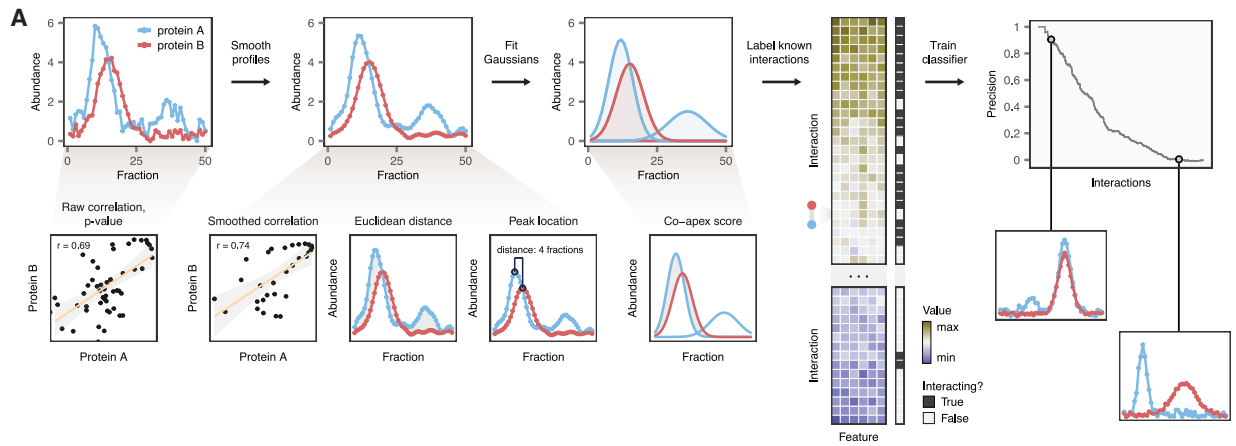
## RESULTS

### Quantitative *in vivo* interactome profiling of mouse tissues

We profiled the interactome of seven mouse tissues, including brain, heart, skeletal muscle (gastrocnemius), lung, kidney, liver, and thymus, using PCP-SILAM ([Figure 1A](#)). The *in vivo* interactome of each tissue was preserved by extracting and separating protein complexes under non-denaturing conditions and in the presence of excess protease and phosphorylase inhibitors. A total of 55 SEC fractions were collected from each tissue, in biological duplicate, from both  $^{13}\text{C}_6$ -labeled (heavy) and unlabeled (light) mice. The heavy fractions were then pooled to generate a global reference mixture, which was

spiked into all 770 light fractions. Each fraction was then subjected to liquid chromatography-tandem mass spectrometry (LC-MS/MS) analysis.

A total of 7,225 unique proteins were detected across all fractions ([Figure 1B](#); [Table S1](#)). The set of identified proteins encompassed many well-known protein complexes, as exemplified by the prefoldin complex, the COP9 signalosome, or the eIF3 complex ([Figure 1C](#)). Notably, PCP-SILAM chromatograms differentiated non-constitutive subunits, such as the loosely bound eIF3j subunit, and complex isoforms, such as the eIF3b-eIF3g-eIF3i submodule ([Valášek et al., 2017](#)). The use of a global reference standard imposed an upper bound on the total number of proteins that could be quantified by their SILAM ratios, as compared to a label-free approach ([Figure S1A](#)). However, the technical



(legend on next page)

precision of SILAM-based protein quantification was significantly higher than that of quantifications based on the light channel only, as quantified either by the coefficient of variation between biological replicates for individual fractions, or the correlation across entire chromatograms (both  $p < 10^{-15}$ , Brunner-Munzel test; Figures S1B and S1C). A small number of protein quantifications were marked by very high ratios relative to the global reference, likely due to a combination of tissue-enriched protein abundance and sharp chromatographic peaks (Figure S1D). However, SILAM continued to afford an increase in quantitative precision even for these very high ratios, supporting the robustness of the technique (both  $p < 10^{-15}$ ; Figures S1E and S1F). Reproducibility between biological replicates was high, with samples clustering by tissue rather than by batch, and no statistically significant batch effects were observed (Figures 1D and 1E; Figures S1G and S1H). Remarkably, the degree of reproducibility we observed was quantitatively comparable to that of cell-line-based PCP-SILAC, despite the greater complexity of *in vivo* tissues (Figure 1F). Reproducibility was somewhat lower for muscle, perhaps because the presence of highly abundant proteins interfered with the identification or quantification of more lowly abundant proteins (Geiger et al., 2013) (Figure S1I).

As an initial assessment of the quality of our data, we compared PCP-SILAM to large-scale proteomics, transcriptomics, and ribosome profiling datasets for their ability to recover known protein complexes (Romanov et al., 2019). Patterns of co-abundance across SEC fractions consistently proved more informative than those in large-scale transcriptome, translato- me, or proteome datasets (Figures 1G and S1J), with a mean area under the ROC curve (AUC) of 0.77, compared to 0.70 for 11 large-scale proteomics studies ( $p = 0.016$ , *t* test), 0.62 for five RNA-seq studies ( $p = 4.9 \times 10^{-5}$ ), and 0.62 in a pair of ribosome profiling studies ( $p = 2.0 \times 10^{-8}$ ). Notably, the mean AUC in PCP-SILAM data was higher than that achieved in a meta-analysis of 5,288 SILAC proteomics experiments from 294 different biological conditions (Kustatscher et al., 2019) (Figure S1K). These findings illustrate the primary advantage of PCP over large-scale proteome “co-regulation” networks: namely, that separation over the SEC column should specifically discriminate pairs of proteins in the same protein complex from indirectly associated pairs,

whose abundance fluctuates in a correlated manner due to involvement in a common underlying biological process. No significant difference in AUC was observed between PCP-SILAM and cell-line-based PCP-SILAC (Figures 1H and S1L;  $p = 0.58$ ), indicating that adaptation for *in vivo* interactome profiling did not compromise data quality, despite the greater complexity of entire tissues.

### Inference of high-confidence mouse tissue interactomes

To derive interactomes from PCP-SILAM tissue proteome profiles, we developed PrInCE, a machine-learning pipeline for analysis of co-fractionation mass spectrometry data (Figure 2A) (Stacey et al., 2017). PrInCE builds on previous approaches to co-fractionation data by training a machine-learning classifier to identify interacting protein pairs, based on the elution patterns of known protein complexes (Havugimana et al., 2012; Wan et al., 2015). However, in contrast to previous approaches that learn jointly from co-fractionation data and publicly available genomic datasets, PrInCE recovers PPIs using features derived exclusively from the mass spectrometric data (Skinnider et al., 2018).

Applying PrInCE to PCP-SILAM data identified between 19,804 and 35,536 interactions in each tissue at a 5% false discovery rate (FDR), for a total of 125,696 unique interactions (Figure 2B; Table S2). Conversely, 47.4% of intra-complex pairs within the training set were not recovered (Figure S2A), suggesting a false negative rate of roughly 50%, at least among intra-complex interactions expected to be detectable by PCP. We tested the robustness of the inferred interactomes by varying the parameters used to perform network inference with PrInCE, finding that the vast majority of interactions were robustly identified (Figure S2B; Table S3). We also evaluated the impact of high SILAM ratios on the inferred networks. Proteins with a high SILAM ratio tended to participate in slightly more tissue-specific interactions, consistent with the notion that these ratios reflect tissue-enriched protein abundance (Figure S2C). However, we also identified high SILAM ratios within well-studied protein complexes, and interactions involving a protein with a high SILAM ratio were recovered at slightly higher precision thresholds than the proteome average, suggesting that these ratios did not hinder accurate network inference (Figures S2D and S2E).

### Figure 2. Inference and validation of mouse tissue interactomes

- (A) Schematic illustration of the computational procedure for interactome network inference from PCP-SILAM data.
- (B) Number and tissue specificity of interactions detected in each mouse tissue.
- (C–E) Comparison of mouse tissue interactomes to high-throughput screens of the human interactome, literature-curated interactions, and known protein complexes.
- (C) Functional coherence of interactome networks. Each vertical band represents a single GO term, shaded by the AUC with which proteins with that GO term could be predicted from network topology alone in each interactome. Vertical lines indicate the proportion of GO terms with AUC less than 0.5, equivalent to random chance.
- (D) Coexpression of interacting protein pairs in quantitative proteomics data from 41 cancer cell lines (Lapek et al., 2017). Each vertical band represents one of 1,000 randomly selected interacting protein pairs, shaded by the coexpression of the two interacting proteins. Vertical lines indicate the proportion of negatively correlated interacting pairs.
- (E) Co-localization of interacting protein pairs, as quantified by their correlation across cellular fractions in subcellular proteomics data.
- (F) PCP-SILAM profiles of talin and the TCP1 complex in the mouse brain and liver.
- (G) Relative abundance of co-immunoprecipitated TCP1 complex subunits to talin in mouse brain and liver. Error bars show standard error across three biological replicates.
- (H) PCP-SILAM chromatograms for Rpl3, Rpl3l, and the 60S ribosome (median and interquartile range, ribbon) in the mouse brain, heart, kidney, and liver.
- (I) Relative abundance of Rpl3 and Rpl3l in purified ribosomes from the same four tissues. Error bars show standard error across four biological replicates. See also Figure S2.

To evaluate the quality of the networks inferred from PCP-SILAM data, we compared each mouse tissue interactome to five recently published high-throughput human interactome screens (Hein et al., 2015; Huttlin et al., 2015, 2017; Luck et al., 2020; Rolland et al., 2014), conducted using AP-MS or Y2H, as well as literature-curated interactions reported in one, two, three, or four publications and well-studied protein complexes. We computed three indices that reflect the concordance of each network with other large-scale genomic datasets. First, we evaluated the functional coherence of the network, defined as the degree to which the function of any given protein can be predicted from those of its interacting partners based on the principle of “guilt by association” (Ballouz et al., 2017; Oliver, 2000). Second, we evaluated the tendency for interacting protein pairs to display correlated patterns of abundance across two large proteomic datasets (Kustatscher et al., 2019; Lapek et al., 2017). Last, we evaluated the degree to which interacting proteins localized to the same subcellular compartments in two subcellular proteomics datasets (Geladaki et al., 2019; Orre et al., 2019) (STAR Methods). All three indices yielded broadly concordant pictures of network quality (Figures 2C, 2E, and S2F–S2H), generally suggesting that interactions inferred by PCP-SILAM were superior to Y2H, comparable or slightly inferior to AP-MS, and intermediate between literature-curated interactions reported in one and two publications. Thus, these findings suggest the quality of PCP-SILAM networks is comparable both to recent systematic human screens and to interactions identified by small-scale, hypothesis-driven experiments.

To validate the tissue specificity of the interactions, we compared the properties of the fitted Gaussians in tissues where an interaction did or did not take place, as inferred by PrInCE. Protein pairs eluted over significantly more distant fractions in tissues where the interaction did not take place ( $p < 10^{-15}$ , Brunner-Munzel test; Figure S2I). Moreover, among protein pairs that did co-elute within a window of two fractions, non-interacting pairs had significantly more variable stoichiometries than interacting protein pairs, suggestive of chance co-elution ( $p < 10^{-15}$ ; Figure S2J). These observations support the notion that PrInCE was able to accurately distinguish tissues in which proteins did or did not interact.

To experimentally validate the ability of PCP-SILAM to map interactions in mouse tissues, we focused on a putative interaction between the cytoskeletal protein talin and the subunits of the chaperonin-containing TCP1 complex, which had not previously been reported in either mouse or human (Figure 2F). Immunoprecipitation of talin confirmed the interaction with TCP1 in mouse brain (Figure 2G). To confirm the tissue specificity of the interaction, we additionally performed immunoprecipitation in mouse liver, where talin and TCP1 complex curves displayed limited correlation, and observed limited co-purification, consistent with PCP-SILAM (Figures 2F and 2G). Similarly, we examined an apparent heart-specific paralog switch in the ribosome, driven by the replacement of the constitutive Rpl3 by its paralog Rpl3l (Figure 2H). Rpl3l is primarily expressed in heart and skeletal muscle, and mutations of Rpl3l are implicated in atrial fibrillation (Thorolfsson et al., 2018). However, it has remained unclear whether Rpl3l is incorporated into ribosomes, or whether its physiological effects are mediated by extra-ribosomal func-

tions (Chaillou et al., 2016). Isolation of purified ribosomes from mouse tissues, followed by label-free quantitation, confirmed the incorporation of Rpl3l into heart-specific ribosomes (Figure 2I). Thus, orthogonal biochemical techniques confirmed the ability of PCP-SILAM to reveal dynamic rearrangements in the interactome across tissues.

### Unbiased expansion of the mouse interactome by PCP-SILAM

The mouse is a ubiquitous model organism, yet its interactome has never been the subject of a systematic, proteome-scale mapping effort. To compare our networks to the known mouse interactome, we assembled a total of 82,602 mouse PPIs that were detected in small-scale experiments from nine interaction databases. Strikingly, of the 125,696 unique interactions detected here by PCP-SILAM, only 4,354 (2.1%) overlap with interactions detected by small-scale experiments (Figure 3A). This overlap is significantly larger than would be expected by chance ( $p < 10^{-15}$ , hypergeometric test) but small in magnitude. We reasoned that this relatively small overlap could likely be explained by two factors: (1) the small size of the known mouse interactome, and (2) the complementarity between PCP-SILAM and the assays employed in small-scale studies. To test the former possibility, we calculated the overlap between our networks and a larger resource of human small-scale interactions. Despite the evolutionary divergence between human and mouse, this overlap was comparable to that observed for recent high-throughput screens of the human interactome, suggesting that the relatively low overlap with the mouse interactome does not reflect an enrichment for false-positives (Figure S3A). We obtained similar results when calculating the overlap with human genetic interactions, which are known to overlap with physical protein-protein interactions (Collins et al., 2007) (Figure S3B). Moreover, we found that among literature-curated PPIs, interactions detected by PCP-SILAM intersected most significantly with those detected by co-sedimentation, and less with PPIs detected by two-hybrid or cross-linking approaches (Figure S3C), supporting the notion that each assay recovers characteristic subsets of the interactome. We additionally asked whether PCP-SILAM exhibits detectable bias toward stable, high-affinity PPIs but found that PCP-SILAM interactions cataloged in the PDBbind database (Liu et al., 2015) spanned a broad range of binding affinities (Figure S3D).

The remaining 121,342 unique interactions detected in this study have not previously been reported in mouse; thus, our proteome-scale resource therefore expands the mouse interactome by a factor of  $\sim 2.5$  (Figure 3B). To functionally characterize these PPIs, we compared patterns of GO term co-annotation between literature-curated and PCP-SILAM interactions (Figure 3C). Relative to literature-curated interactions, mouse PPIs detected by PCP-SILAM were enriched for connections involving metabolism, translation, and protein folding. In contrast, PCP-SILAM PPIs were underrepresented in connections involving cell-cell signaling and proliferation. These findings are broadly consistent with the expectation that PCP-SILAM would prioritize cytosolic over nuclear or extracellular complexes.

We next asked whether PPIs detected by PCP-SILAM preferentially expanded existing regions of the global mouse

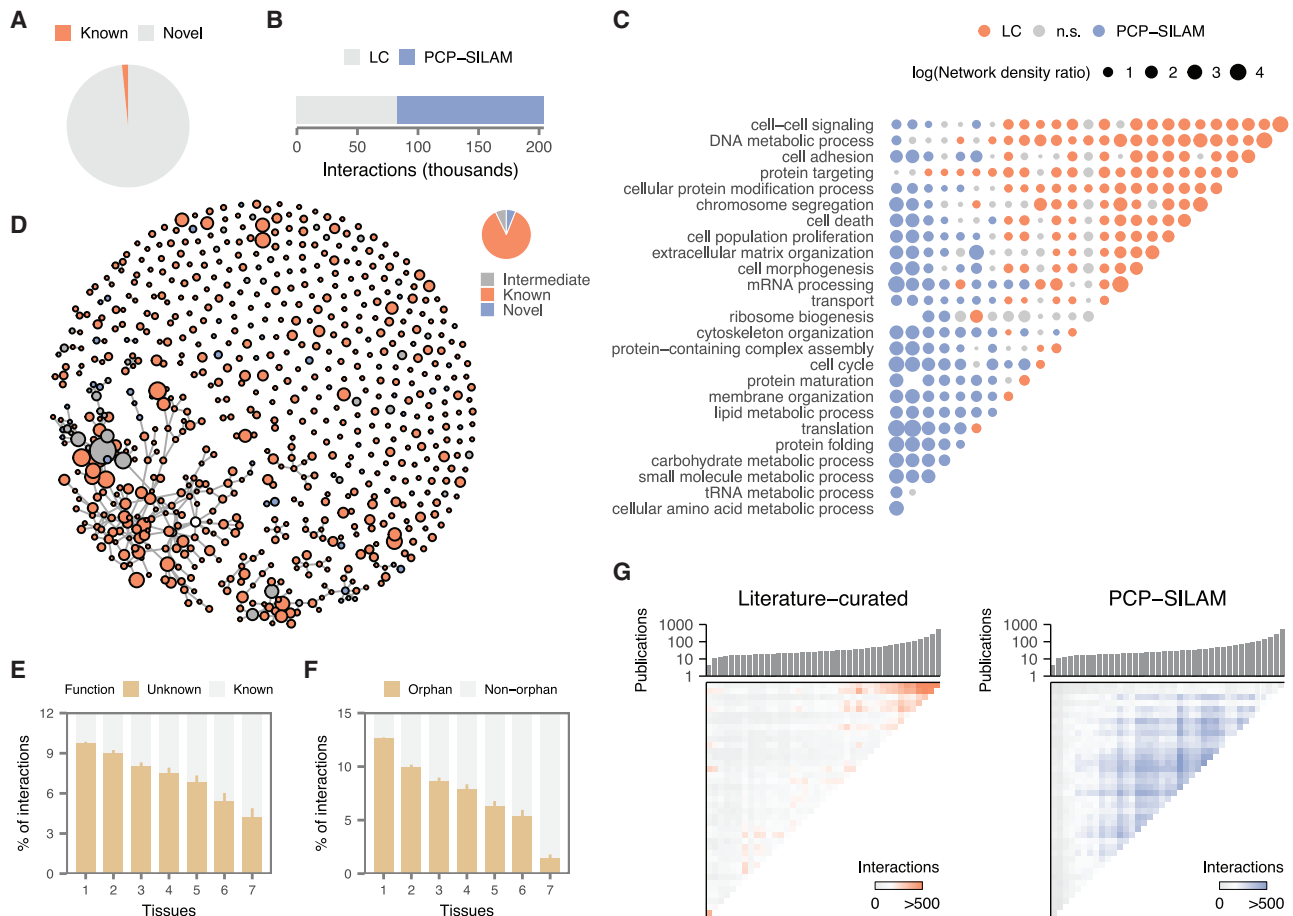


**Figure 3. Unbiased expansion of the literature-curated mouse interactome by PCP-SILAM**

(A) Proportion of previously known mouse interactions observed in PCP-SILAM tissue interactomes.  
 (B) Size of the known mouse interactome before and after this study.  
 (C) Comparison of interacting protein co-annotation within and across biological processes between PCP-SILAM and LC interactions.  
 (D) Markov clustering of the global mouse interactome, and proportion of protein communities containing exclusively known interactions (“known”), exclusively PCP-SILAM interactions (“novel”), or both (“intermediate”).  
 (E) Proportion of interactions involving proteins of unknown function, among interactions detected in one to seven tissues.  
 (F) Proportion of interactions involving interactome orphans, among interactions detected in one to seven tissues.  
 (E and F) Error bars show the standard error of the sample proportion.  
 (G) Number of interactions between proteins binned by number of publications, and ordered along both axes. Histogram shows the median number of publications in each bin.  
 See also [Figure S3](#).

interactome, or tended to form distinct subnetworks. To provide a global view of network topology, we applied Markov clustering (Enright et al., 2002) to group the entire mouse interactome, including both literature-curated and PCP-SILAM interactions, into 696 clusters (Figure 3D; Table S4). Of the 92 clusters containing at least one PPI detected by PCP-SILAM, 50 (54%) included both literature-curated and high-throughput PPIs, while 42 were composed exclusively of PCP-SILAM interactions. Thus, while PCP-SILAM reveals several protein communities that were altogether unknown in mouse, many interactions also expand neighborhoods of the mouse interactome with foundations previously defined by small-scale experiments.

Literature-curated protein interaction datasets have been criticized on the grounds that they are biased toward a relatively

small set of highly studied proteins. We organized the literature-curated mouse interactome by ranking proteins based on the number of publications in which they have been mentioned, as in a previous study of the human interactome (Rolland et al., 2014), and found that the mouse literature-curated interaction dataset is likewise dominated by interactions between well-studied proteins (Figure 3G). High-throughput interactome mapping studies provide a means to define the architecture of the proteome independent of investigator biases, and in comparison to the literature-curated dataset, PPIs detected by PCP-SILAM are distributed more homogeneously (Figure 3G). However, we anticipated that the untargeted nature of our *in vivo* approach could result in a reduced capacity to detect interactions for lowly expressed proteins, compared to targeted approaches. To test

this notion, we re-organized both the literature-curated and PCP-SILAM interactomes by protein abundance (Schwanhäusser et al., 2011). Consistent with this expectation, PPIs detected by PCP-SILAM displayed a moderate bias toward more abundant proteins, whereas interactions detected by small-scale experiments largely did not (Figure S3E).

To date, large-scale mammalian interactome mapping projects have typically been performed in yeast or cell lines (Snider et al., 2015). However, many biologically relevant PPIs may not occur within these systems. We therefore hypothesized that mapping the *in vivo* interactome in physiological contexts, such as in individual tissues, could preferentially reveal novel interactions. Consistent with this hypothesis, we found that tissue-specific interactions were significantly less likely to have been cataloged in literature-curated interaction databases (Figure S3F;  $p < 10^{-15}$ , Kendall rank correlation), likely because few small-scale studies have taken place *in vivo*. We also investigated whether mapping interactomes in mouse tissues could preferentially provide insights into interactions involving proteins whose functions are poorly understood. PCP-SILAM identified interacting partners for 218 proteins of unknown function (Table S5A), and these interactions were significantly more tissue specific than the interactome average (Figure 3E;  $p < 10^{-15}$ , Kendall rank correlation). Similarly, we mapped interactions involving 366 proteins for which no interacting partners had previously been detected (interactome “orphans,” Table S5B) (Kotlyar et al., 2015) and found that these interactions likewise displayed a significant trend toward increasing tissue specificity (Figure 3F;  $p < 10^{-15}$ , Kendall rank correlation). Thus, mapping the *in vivo* interactome of mammalian tissues can shed light on poorly studied components of the proteome.

### Widespread interactome rewiring limits the accuracy of tissue-specific interactome prediction

In the absence of experimental tissue- or cell-type-specific interactomes, computational methods have been developed to predict context-specific molecular interaction networks (Greene et al., 2015; Marbach et al., 2016). The most widely used strategy for context-specific interactome prediction proceeds from the notion that the protein products of two genes can only interact in a given context if these genes are both expressed. Gene or protein expression data are overlaid onto a static interactome, and the subset of the network whose nodes are expressed above a certain threshold is extracted to generate the context-specific interactome (Figure 4A) (Bossi and Lehner, 2009; Buljan et al., 2012; de Lichtenberg et al., 2005). For instance, human tissue transcriptome data from the GTEx project overlaid onto a draft map of the human interactome by Y2H (Luck et al., 2020) to infer tissue-specific networks. An alternative strategy is to construct tissue-specific gene coexpression networks, which suggest functional association in a given tissue, if not necessarily physical interaction (Pierson et al., 2015; Saha et al., 2017; Voineagu et al., 2011; Zhang et al., 2013). However, the degree to which predictions made by these methods capture physiologically relevant interactome rearrangements is unclear.

Using our PCP-SILAM mouse tissue interactomes as a reference, we investigated the accuracy of these approaches in predicting tissue-specific interactomes. We calculated the overlap between the predicted and PCP-SILAM tissue interactomes

and then compared this overlap to that observed for randomly rewired networks. Surprisingly, tissue interactomes predicted based on gene expression were only 2- to 4-fold enriched for experimentally detected interactions, relative to randomized networks (range, 2.3–4.1; Figure 4B). This overlap was highly significant, but small in magnitude. Overlaying protein or phosphoprotein abundance onto static networks, instead of gene expression, did not substantially improve the overlap (Figure S4A). Similarly modest enrichment was observed for tissue-specific coexpression networks (Figure 4B), consistent with previous findings that gene coexpression is a relatively poor predictor of physical interaction (Fortelny et al., 2017; Kühner et al., 2009). Thus, neither tissue-specific gene or protein expression, nor coexpression, are sufficient to accurately predict tissue-specific physical PPIs.

Predicted tissue interactomes also differed markedly in their topology from experimentally determined interactomes. In interactome networks, the most highly connected (“hub”) proteins are slow evolving and physiologically indispensable (Fraser et al., 2002; Jeong et al., 2001). The hub proteins of predicted tissue interactomes were highly consistent across tissues, with 65%–70% of hubs in each tissue shared between all predicted networks (Figure 4C). However, we found that hub proteins were much less consistent *in vivo*, with only 20 hubs shared across all tissues (Figure 4C). Moreover, this trend could not be attributed to differences in proteome coverage between tissues, as most hub proteins were present in all tissue interactomes but differed specifically in their connectivity (Figure S4B). The identities of the hub proteins themselves in each tissue were also poorly predicted, with only 3.7%–5.9% of hub proteins overlapping between predicted and *in vivo* interactomes (Figure S4C). More generally, the number of interactions in which any given protein participates (its degree) was considerably more variable across tissues in *in vivo* interactomes than in predicted networks (Figures 4D, S4D, and S4E). Similarly, proteins displayed a much greater tendency to interact with different partners across tissues than was predicted by gene expression alone (Figures 4E and S4F). These results can be rationalized on the basis that, in predicted tissue interactomes, a protein expressed in a given tissue retains all of its interactions with other proteins expressed in that tissue, since differences in degree can be caused solely by absence of the protein or its partners from the tissue in question. Consequently, both the degree of proteins in the network, as well as the specific identities of their interacting partners, remain artificially stable across tissues.

Taken together, these analyses reveal widespread rewiring of interactome networks across mouse tissues beyond what is apparent from gene expression alone, affecting both the specific interactors of individual proteins and the global topological properties of physiological interactomes. Critically, the observation that a pair of proteins can interact in at least one context does not imply that their expression in a second context is a sufficient condition to reproduce the interaction. For example, PCP-SILAM correctly identified the known interaction between the F-actin-capping protein (CapZ) and the CapZ-interacting protein (CapZIP or Rcsd1) (Edwards et al., 2014; Eyers et al., 2005). However, the interaction was specific to heart and muscle, despite robust expression of the interacting proteins in all seven tissues

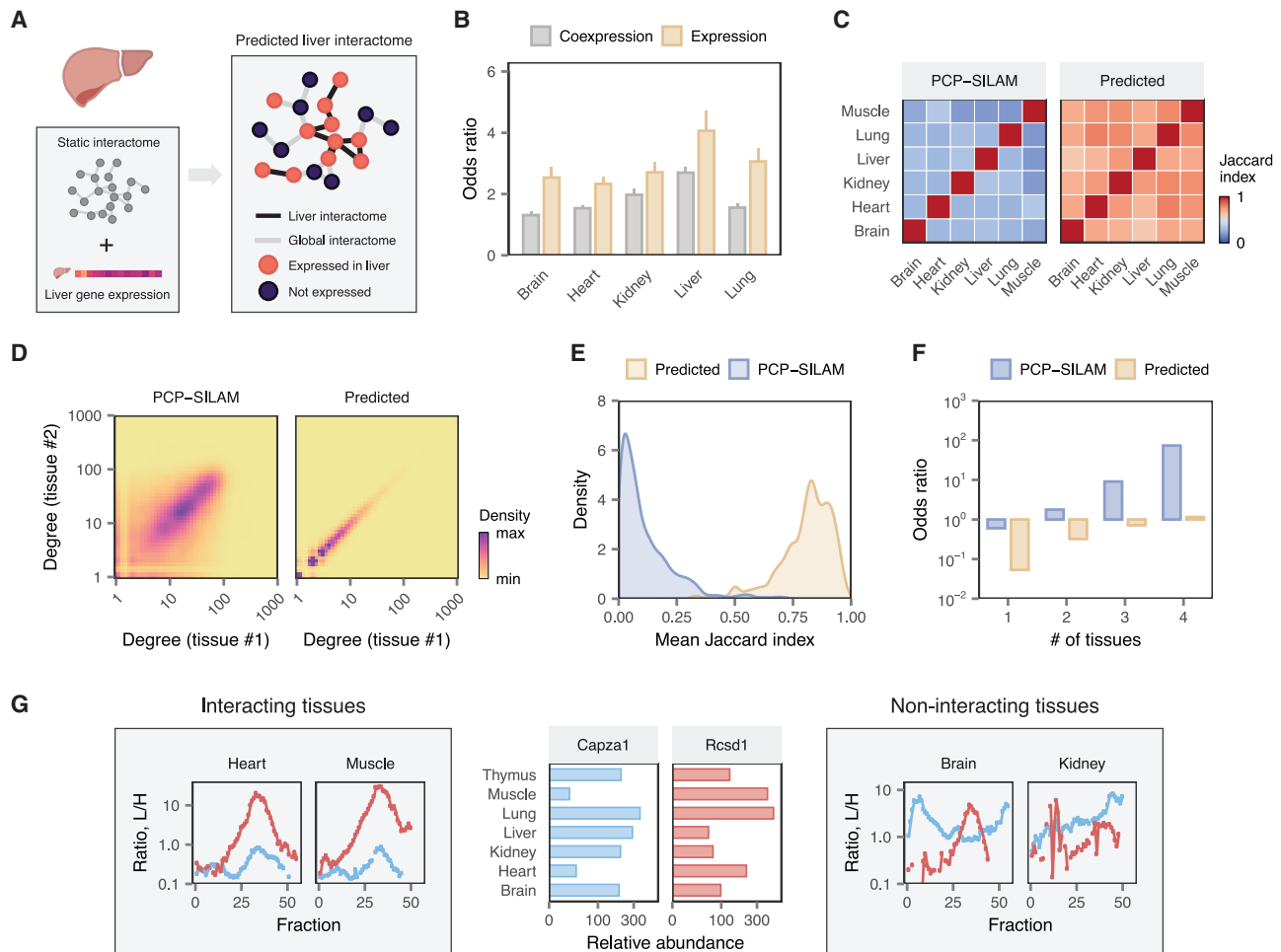


**Figure 4. Interactome rewiring limits accuracy of tissue-specific interactome prediction**

(A) Schematic illustration of tissue interactome prediction by integration of static interactome maps with tissue-specific gene-expression profiles.  
 (B) Overlap between PCP-SILAM mouse tissue interactomes and tissue-specific gene coexpression networks or tissue interactomes predicted based on gene expression, relative to rewired networks. Error bars show the standard deviation.  
 (C) Overlap in hub proteins across tissues in predicted and PCP-SILAM tissue interactomes.  
 (D) Variability in protein degree across tissues in predicted and PCP-SILAM tissue interactomes.  
 (E) Protein rewiring across tissues in predicted and PCP-SILAM tissue interactomes, as quantified by the mean Jaccard index of each protein across all tissue pairs.  
 (F) Enrichment for interactions found in one to four tissues in predicted and PCP-SILAM tissue interactomes, relative to randomized networks.  
 (G) PCP-SILAM profiles reveal Rcsd1 and Capza2 interact in heart and muscle, but not brain or kidney, despite expression in all seven tissues. Left, PCP-SILAM chromatograms for Rcsd1 (red) and Capza2 (blue) in heart and muscle. Middle, summed SILAM ratios for Capza2 and Rcsd1 in each tissue. Right, PCP-SILAM chromatograms in brain and kidney.  
 See also [Figure S4](#).

([Figure 4G](#)). This pattern of tissue specificity could not have been predicted on the basis of protein expression alone. To evaluate whether predicted interactomes are depleted for tissue-specific interactions more systematically, we randomized interaction networks for each tissue separately and calculated the total number of interactions found across one to seven randomized tissue interactomes. Consistent with the expectation that gene expression alone would underestimate the degree of interactome variability across tissues, predicted interactomes were significantly depleted for the most tissue-specific interactions, relative to PCP-SILAM interactomes ([Figures 4F and S4F](#);  $p < 10^{-15}$ , Z test).

### Evolution of interactions in mammalian tissues

Extrapolation of physical interactions detected in one organism to orthologous pairs of proteins in a different organism has been widely used to predict the interactomes of non-model organisms, or increase coverage of the human interactome ([Li et al., 2017](#); [Matthews et al., 2001](#); [Yu et al., 2004](#)). However, tissues may execute specialized biological functions that are less conserved between organisms than ubiquitous “housekeeping” processes ([Zhang and Li, 2004](#)). We hypothesized that more tissue-specific interactions would show less evidence of evolutionary conservation than those occurring across many tissues.

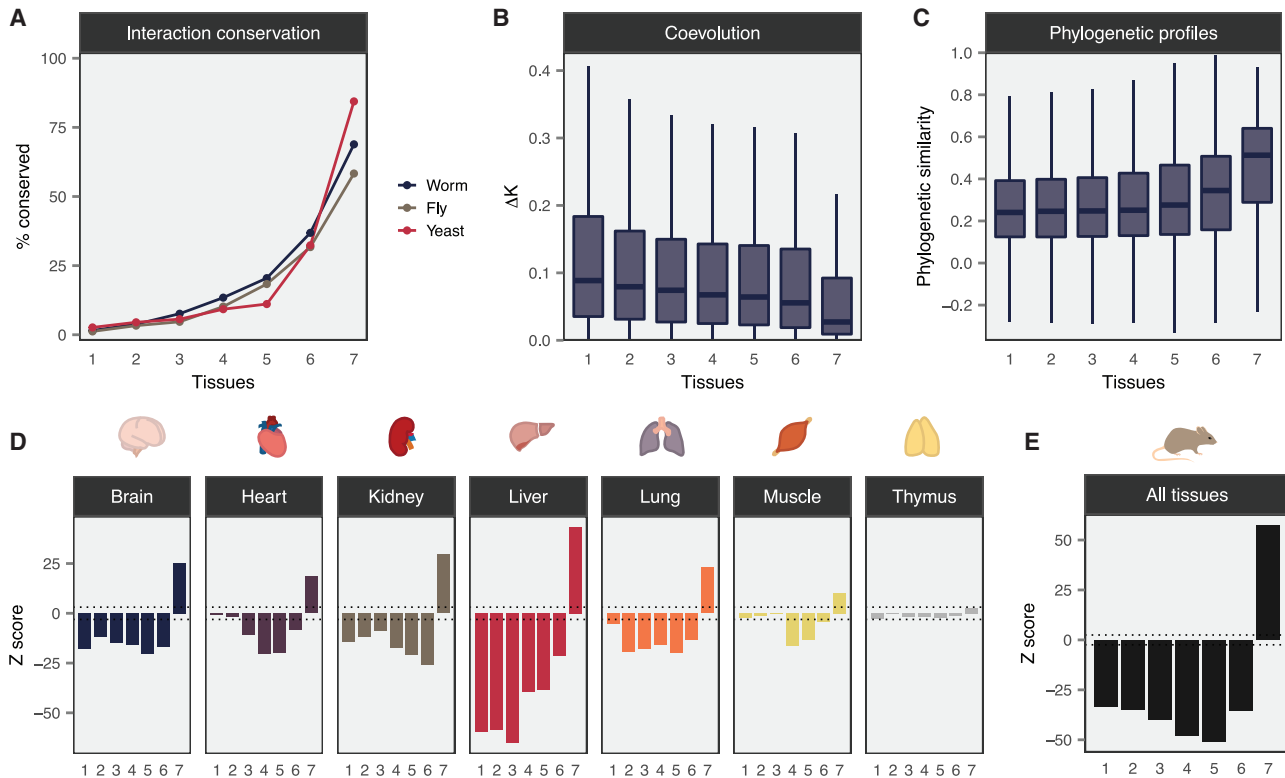


**Figure 5. Evolution of mammalian tissue interactomes**

(A) Proportion of mouse interactions conserved in worm, fly, and yeast for interactions detected in one to seven tissues.

(B) Differences in evolutionary rates between interacting protein pairs detected in one to seven tissues.

(C) Correlations in phylogenetic profiles between interacting protein pairs detected in one to seven tissues.

(D and E) Connectivity between housekeeping proteins and proteins quantified in one to seven tissues, in each mouse tissue interactome (D) and aggregated across mouse tissues (E), expressed as a Z score relative to randomly rewired networks.

See also [Figure S5](#).

Examining literature-curated interactions for three model organisms, and five recent human high-throughput interactome screens, we found that tissue-specific interactions were less likely to be evolutionarily conserved (Figures 5A and S4A;  $p < 10^{-15}$  for model organisms and humans respectively, Fisher integration of Kendall rank correlations). Protein pairs that made tissue-specific interactions likewise co-evolved at less similar rates (Figure 5B;  $p < 10^{-15}$ , Kendall rank correlation), and had less correlated patterns of presence and absence across eukaryotic genomes (Figure 5C;  $p < 10^{-15}$ ) relative to universal interactions (Fraser et al., 2002; Pellegrini et al., 1999). Thus, both experimental screens and large-scale genomic data highlight the evolutionary novelty of tissue-specific interactions.

We next asked whether tissue-specific interactions predominantly arise from tissue-specific rewiring of ancient proteins, or whether they instead involve evolutionarily young proteins. Relative to universal interactions, tissue-specific interactions disproportionately involved younger proteins (Figure S5B;  $p < 10^{-15}$ ). Furthermore, ancient proteins had more conserved interaction partners across tissues, whereas younger proteins were disproportionately rewired between tissue interactomes (Figure S5C;  $p < 10^{-15}$ ), suggesting that rewiring of ancient proteins is insufficient to explain the evolution of new tissue-specific interactions.

Previous analyses of predicted tissue interactomes identified extensive interactions between proteins expressed in only a subset of tissues and those expressed in all tissues (housekeeping proteins), proposing a model wherein tissue-specific functions arise by recruiting core cellular processes (Bossi and Lehner, 2009). Motivated by our observation that interactome rewiring is poorly predicted by tissue-specific gene expression, we investigated whether PCP-SILAM data supported this model. To quantify the extent of cross-talk between housekeeping and tissue-specific proteins, we randomly rewired each tissue interactome and compared the number of interactions between proteins at each level of tissue specificity to the number observed in randomized networks (Figure S5D). In every tissue, housekeeping proteins displayed highly significant enrichment for interactions with other housekeeping proteins (Figure 5D). In contrast, we observed systematic depletion of interactions between tissue-specific and housekeeping proteins compared to randomized networks, particularly when aggregating results across all seven tissues (Figure 5E). Experimental tissue interactome mapping therefore suggests that evolutionarily novel tissue-specific interactions accomplish tissue-specific functions largely independent of the core modules of universal interactions.

Taken together, these analyses contrast two systems: core cellular modules present across all mouse tissues, and accessory modules that execute specialized functions within individual tissues. The former involves ancient proteins that have co-evolved over long evolutionary time frames, and whose interaction partners are preserved across species and tissues. In contrast, tissue-specific interactions are less often conserved in other species and disproportionately involve younger proteins. Remarkably, we observe suppression of cross-talk between these two systems, with significant depletion of interactions between tissue-specific and universal proteins.

### Tight regulation of tissue-specific interaction rewiring

Having established that evolutionarily ancient proteins have significantly more stable interaction partners across tissues than the interactome average, we sought to further characterize the properties of proteins whose interactions are disproportionately rewired in a tissue-specific manner. To quantify the degree of interaction rewiring across tissues for each protein, we compared the similarity of its interaction partners across all pairs of tissues using the Jaccard index (Figure 6A). Proteins with a higher Jaccard index participate in interactions that are preserved across mouse tissues, whereas proteins with a low Jaccard index have interaction partners that are more rewired.

As expected, members of known protein complexes were significantly less rewired across tissues (Figure 6B;  $p < 10^{-15}$ , one-tailed Brunner-Munzel test). However, GO enrichment analysis failed to identify functional categories overrepresented among rewired proteins. We therefore asked whether protein structural features instead would be predictive of rewiring. We hypothesized that intrinsically disordered proteins, which lack a unique structure, would possess the increased interaction surface area and conformational flexibility necessary to interact with multiple target proteins. Indeed, disordered proteins were significantly more rewired than their structured counterparts (Figure 6C;  $p = 7.8 \times 10^{-7}$ ). Disordered protein segments often embed short peptide interaction motifs that can be bound by globular domains (Davey et al., 2012), and proteins containing such linear motifs were likewise significantly more rewired (Figure 6D;  $p = 1.3 \times 10^{-6}$ ). Intrinsically disordered regions are also known to be hotspots for protein phosphorylation (Iakoucheva et al., 2004), raising the possibility that interaction rewiring may be coordinated by tissue-specific post-translational modification. Consistent with this possibility, phosphoproteins were enriched among rewired proteins (Figure 6E;  $p = 3.7 \times 10^{-4}$ ), and phosphosites on rewired proteins were significantly more tissue-specific than those found on universal proteins (Figure S6A;  $p = 7.3 \times 10^{-5}$ , Spearman rank correlation). Partial correlation analysis confirmed the enrichments for both linear motifs and phosphosites were independent of intrinsic disorder ( $p = 1.2 \times 10^{-3}$  and  $6.0 \times 10^{-3}$ , respectively). Collectively, these findings suggest that binding motifs and post-translational modification sites embedded within intrinsically disordered regions facilitate the rewiring of protein interaction partners across mammalian tissues.

Disordered proteins are frequently involved in signaling pathways or mediate regulatory functions (Ward et al., 2004). We therefore hypothesized that rewiring of PPIs across tissues could

facilitate tissue-specific signaling processes. Consistent with this hypothesis, tissue-specific interactions were significantly more likely to involve protein kinases, transcription factors, and cell-surface protein receptors (Figures S6B–S6D;  $p < 10^{-15}$ ,  $p = 5.5 \times 10^{-13}$ , and  $p = 2.0 \times 10^{-5}$ , respectively, Kendall rank correlation). In addition, we calculated the betweenness centrality of each interaction, defined as the number of shortest paths across the network that pass through each edge. Edges with a high betweenness centrality in interactome networks are associated with information flow across the network (Yan et al., 2016), and, in agreement with this notion, we found tissue-specific interactions to have a significantly higher centrality than universal interactions (Figure 6F;  $p < 10^{-15}$ , Kendall rank correlation). Thus, both molecular and network topological perspectives highlight the key role of tissue-specific interactions in propagating biological information within tissue-specific pathways.

Within the cell, precise coordination of macromolecular interactions is required for accurate transmission of biological information. We therefore hypothesized that proteins whose interaction partners are highly variable across physiological contexts would be subject to tight regulatory mechanisms and asked whether specific cellular strategies regulate the availability of rewired proteins. mRNAs encoding rewired proteins were expressed at lower levels, had shorter half-lives, and were transcribed at slower rates (Figures S6E–S6G;  $p = 2.5 \times 10^{-14}$ ,  $4.6 \times 10^{-5}$ , and  $1.7 \times 10^{-13}$ , respectively, Spearman rank correlation) than proteins with more stable interaction partners. Rewired proteins themselves were also less abundant (Figure 6G;  $p < 10^{-15}$ ), and this difference in abundance was controlled both by a reduced rate of translation and increased rate of degradation (Figures 6H and 6I; both  $p < 10^{-15}$ ), suggesting multiple cellular mechanisms converge to tightly regulate the abundance of proteins whose interacting partners are rewired across tissues. Disordered proteins are known to be tightly regulated (Gspöner et al., 2008), but partial correlation analysis confirmed the tight regulation of rewired proteins was independent of protein disorder for all outcomes ( $p \leq 5.0 \times 10^{-6}$ , partial Spearman correlation). Moreover, to rule out the possibility that these associations reflected technical limitations in the identification or quantification of low-abundance proteins, we re-calculated the Jaccard index after excluding low-abundance proteins or proteins identified in only a subset of tissues, finding that all associations remained significant (all  $p \leq 1.8 \times 10^{-3}$ , Spearman rank correlation; Figure S6H).

Given this tight regulation of rewired proteins, we further asked whether proteins whose interaction partners are highly rewired between tissues were associated with deleterious phenotypes. Remarkably, we found that disease genes were significantly more rewired across tissues than the interactome average (Figure 6J;  $p = 1.1 \times 10^{-2}$ ). Many human diseases are caused by germline mutations that are present in virtually every cell in the body, but which manifest in pathology in only one or a handful of tissues (Lage et al., 2008). We therefore drew on a resource of disease genes linked to tissue-specific pathologies (Basha et al., 2020) to ask whether the protein products of these genes are preferentially interconnected in the interactomes of the disease-associated tissues, as has long been hypothesized (Barshir et al., 2014; Hekselman and Yeger-Lotem, 2020; Kitsak et al.,

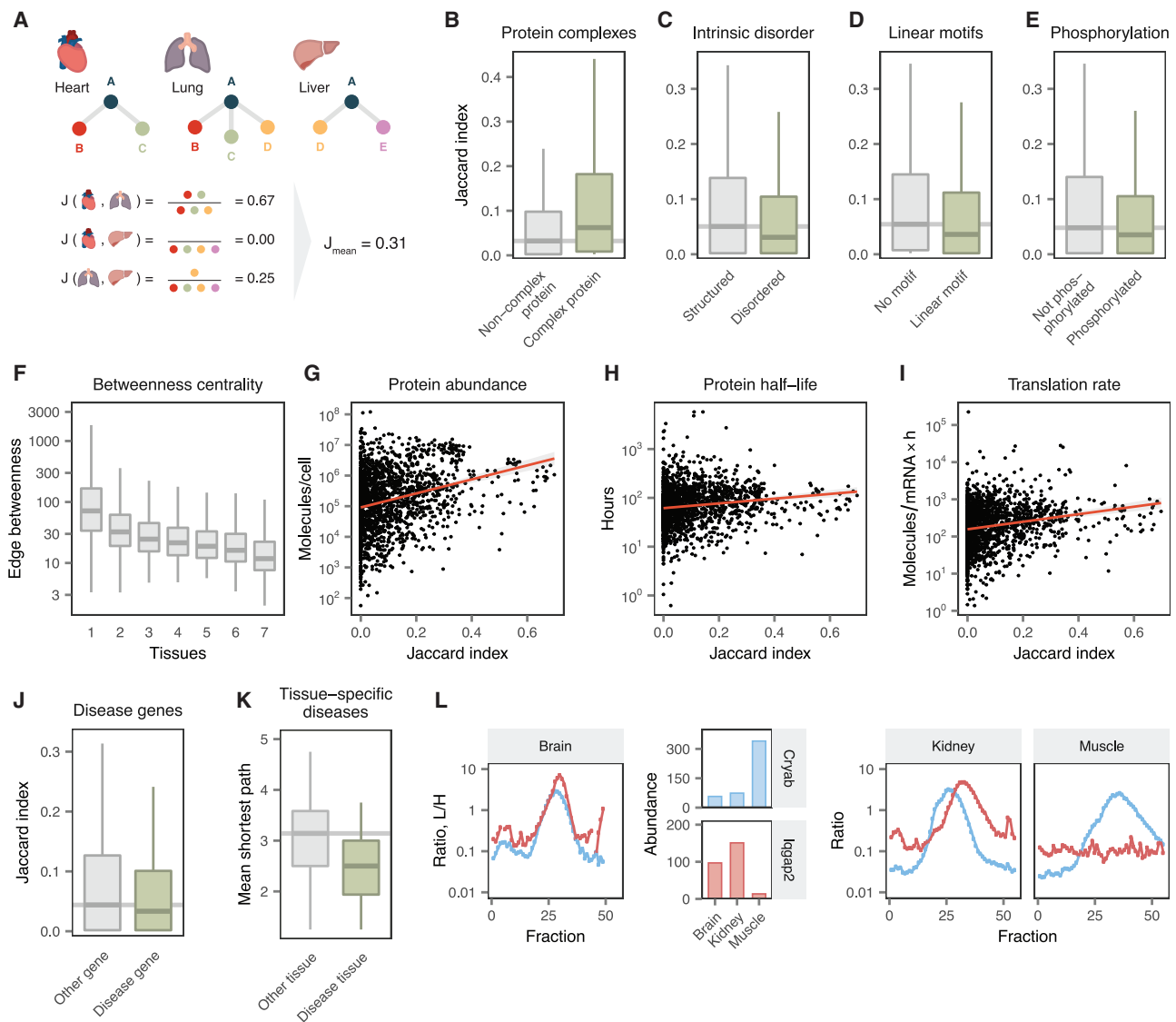


**Figure 6. Tight regulation of interaction rewiring**

(A) Schematic overview of the mean Jaccard index calculation.

(B) Members of known protein complexes display a lesser degree of interaction rewiring across tissue interactomes.

(C) Intrinsically disordered proteins display a greater degree of interaction rewiring across tissue interactomes.

(D) Proteins containing protein-binding linear motifs display a greater degree of interaction rewiring across tissue interactomes.

(E) Phosphoproteins display a greater degree of interaction rewiring across tissue interactomes.

(F) Betweenness centrality of interactions detected in one to seven tissues.

(G–I) Rewired proteins are characterized by low abundance (G), short half-lives (H), and slow translation rates (I).

(J) Disease genes display a greater degree of interaction rewiring across tissue interactomes.

(K) Disease genes associated with diseases that manifest in a specific tissue are more interconnected in the disease-associated tissue than in non-matched tissues.

(L) PCP-SILAM detects a brain-specific interaction between Iqgap2 and Cryab, an intrinsically disordered protein and disease gene.

See also [Figure S6](#).

2016; Magger et al., 2012). Indeed, the mean shortest paths between disease genes were significantly smaller in disease-associated tissues (Figure 6K;  $p = 5.4 \times 10^{-4}$ ), indicating the formation of tissue-specific disease modules (Menche et al., 2015a). The interaction between Cryab, a heat shock protein with an intrinsically disordered C-terminal segment implicated in a number of neuro-

logical disorders (Baldwin et al., 2012; Kuipers et al., 2017), and Iqgap2, a multifunctional signaling protein required for axon outgrowth (Wang et al., 2007), provides an example of disease gene rewiring between tissues. PCP-SILAM detected the interaction in brain, but not kidney or muscle, despite robust expression of the interacting proteins in all three tissues (Figure 6L).

Taken together, these analyses highlight the role of protein-binding motifs and post-translational modification sites within disordered regions in mediating interaction rewiring across physiological contexts. The resulting tissue-specific interactions are associated with transmission of biological information in tissue-specific signaling pathways. Highly rewired proteins are subject to tight regulation by multiple convergent cellular mechanisms, perhaps to ensure the fidelity of biological information flow, and the elevated rate of interaction rewiring among disease genes implicates dysfunction of this regulatory cascade in disease pathophysiology. Notably, disease genes are preferentially interconnected in the interactomes of the tissues in which disease manifests, suggesting that mapping context-specific interactomes will be critical to elucidate the disease modules underlying pathobiology (Menche et al., 2015a).

## DISCUSSION

Charting the complete protein-protein interactome is essential to revealing the molecular origins of cellular processes. However, earlier efforts produced static interactome maps that are fundamentally limited with respect to understanding interaction rewiring across tissue- or cell-type-specific contexts. By applying PCP-SILAM to map the *in vivo* interactomes of seven mouse tissues, we provide a systematic, proteome-scale resource to understand the dynamic physiological interactome. We provide an interactive web application to facilitate exploration of the complete dataset, available at <https://tissue-interactomes.msl.ubc.ca/>.

In the absence of high-throughput methods to define context-specific *in vivo* interactomes, computational methods have been developed to predict interactome rewiring based on gene expression (Bossi and Lehner, 2009; Buljan et al., 2012; de Lichtenberg et al., 2005). We find that widespread and physiological interactome rewiring limits the accuracy of tissue interactome predictions based on patterns of gene expression or coexpression. The result is that these predicted networks bear little resemblance to those we observe in biological tissues, given the opportunity to make such observations experimentally. Together, these findings reinforce conclusions from targeted studies, which have revealed marked dissimilarities in PPIs across cell lines (Floyd et al., 2016; Jäger et al., 2011), between cellular compartments (Markmiller et al., 2018), in response to cellular stimulation (Kerr et al., 2020; Kristensen et al., 2012), or in disease-relevant contexts (Pankow et al., 2015; Shirasaki et al., 2012). In yeast, widespread interaction rewiring has been observed in response to environmental perturbations (Celaj et al., 2017; Liu et al., 2020). Our systematic screen builds on these findings, revealing interactome rewiring at a much larger scale and across healthy mammalian tissues.

Evolutionary analyses of mouse tissue interactomes contrast core cellular modules composed of evolutionarily ancient proteins that are connected via universal interactions with evolutionarily recent proteins that interact in a more tissue-specific manner and are associated with cellular signaling. Intrinsically disordered proteins are particularly predisposed to interaction rewiring across tissues, consistent with the notion that these proteins can adopt new interacting partners over rapid evolu-

tionary timescales (Hultqvist et al., 2017). Our findings linking proteins containing linear motifs or intrinsically disordered regions to an *in vivo* program of interactome rewiring substantiate previous bioinformatic or *in vitro* analyses, which suggested that alternative splicing of disordered protein-coding exons can facilitate interactome remodeling (Buljan et al., 2012; Ellis et al., 2012; Romero et al., 2006). Proteins whose interactions are highly rewired across tissues are subject to tight cellular regulation and are implicated in disease, suggesting dysfunction of this regulatory program may underlie deleterious phenotypes. Intriguingly, topological analyses reveal the formation of tissue-specific disease modules for genes implicated in tissue-specific pathologies, potentially explaining the phenomenon whereby mutations present in every cell in the body lead to dysfunction in only a subset of tissues.

The quantitative proteomic method presented in this study, PCP-SILAM, has the advantage of being an untargeted and relatively unbiased technique, apart from its moderate bias toward proteins of higher cellular abundance. As a high-throughput technique for *in vivo* interactome mapping, PCP-SILAM is uniquely suited to the discovery of interactions across multiple physiological conditions. To date, related co-fractionation mass-spectrometry approaches have primarily been applied to identify evolutionarily conserved protein-protein interactions by acquiring data from multiple species (McWhite et al., 2020; Wan et al., 2015), or to analyze interactome rewiring in response to a stimulus within a single cell line (Heusel et al., 2020; Kerr et al., 2020; Kristensen et al., 2012; Scott et al., 2015, 2017). Our work extends these co-fractionation approaches to interrogate interactome rewiring across multiple tissues *in vivo*. The resulting interactomes access previously unmapped regions and functional classes within the mouse interactome, and place poorly studied mouse proteins into tissue-specific functional contexts, suggesting PCP-SILAM will be a valuable method to shed light on poorly understood components of the proteome.

Whereas our analytical approach to characterizing interactome rewiring took the form of comparing inferred networks across tissues, the use of a global reference mixture in PCP-SILAM expectantly provides a basis for a more quantitative comparison of interaction dynamics. Emerging “complex-centric” analysis strategies take advantage of the information provided by co-fractionation mass spectrometry to quantify protein complex abundance and stoichiometry (Bludau et al., 2020; Heusel et al., 2019), and the technical precision of PCP-SILAM should provide excellent support for such analyses. At present, however, these strategies are designed primarily for the analysis of known interactions. Approaches that extend complex-centric paradigms to the simultaneous discovery and quantification of novel interactions (Rosenberger et al., 2020) will likely add further resolution to co-fractionation datasets in future work.

## Limitations of the study

Some limitations of the present study should be noted. First, we find that the technical precision of protein quantifications based on SILAM ratios is high, in comparison to quantifications based on the light channel only. However, this comparison is limited by the fact that the dynamic range of protein quantification would expectantly be higher in an experiment without any

isotopic labeling, precluding a true head-to-head comparison with a label-free experiment. A second consideration that bears emphasis is that while the vast majority of the 125,00 unique interactions identified here had not previously been reported in mouse, some of them had been previously identified in human. A broader limitation is that the seven tissues analyzed here are each composed of multiple distinct cell types, which expectantly also have their own cell-type-specific interactomes. Future efforts will be necessary to increase the resolution of *in vivo* interactome mapping to the level of cellular subpopulations.

## STAR★METHODS

Detailed methods are provided in the online version of this paper and include the following:

- **KEY RESOURCES TABLE**
- **RESOURCE AVAILABILITY**
  - Lead contact
  - Materials availability
  - Data and code availability
- **EXPERIMENTAL MODEL AND SUBJECT DETAILS**
- **METHOD DETAILS**
  - SILAM incorporation monitoring
  - Tissue harvesting
  - Preparation of cytoplasmic complexes
  - In-solution digestion
  - Mass spectrometry
  - Co-immunoprecipitation
  - Ribosome isolation
- **QUANTIFICATION AND STATISTICAL ANALYSIS**
  - Proteomic data analysis
  - Interactome network inference
  - Comparison to published interactomes
  - Literature-curated interactions
  - Predicted tissue interactomes
  - Evolutionary analysis of tissue interactomes
  - Interaction rewiring across tissues

## SUPPLEMENTAL INFORMATION

Supplemental information can be found online at <https://doi.org/10.1016/j.cell.2021.06.003>.

## ACKNOWLEDGMENTS

This work was supported by funding from Genome Canada and Genome British Columbia (projects 214PRO and 264PRO to L.J.F.) and the Canadian Institutes of Health Research (MOP77688 to L.J.F.), and by computational resources provided by WestGrid Compute Canada, and Advanced Research Computing at the University of British Columbia. M.A.S. acknowledges support from a CIHR Vanier Canada Graduate Scholarship, an Izaak Walton Killam Memorial Pre-Doctoral Fellowship, a UBC Four Year Fellowship, and a Vancouver Coastal Health–CIHR–UBC MD/PhD Studentship. N.E.S. was supported by a Michael Smith Foundation Post-doctoral Fellowship (award #5363) and a National Health and Medical Research Council of Australia (NHMRC) Overseas (Biomedical) Fellow (APP1037373). The authors thank Allison McAfee for constructive comments on the manuscript, Dmitry Vavilov for assistance with the web server, and the Melbourne Mass Spectrometry and

Proteomics Facility of the Bio21 Molecular Science and Biotechnology Institute at the University of Melbourne for mass spectrometry support.

## AUTHOR CONTRIBUTIONS

Conceptualization, M.A.S., N.E.S., J.G., and L.J.F.; methodology, M.A.S., N.E.S., A.P., C.H.K., R.G.S., J.G., and L.J.F.; formal analysis, M.A.S., N.E.S., R.G.S.; investigation, N.E.S., A.P., C.H.K., N.S., Q.W.T.C., and D.R.; writing – original draft, M.A.S., N.E.S., J.G., and L.J.F.; writing – review & editing, M.A.S., N.E.S., A.P., C.H.K., N.S., R.G.S., J.G., and L.J.F.; funding acquisition, L.J.F.; supervision, J.G. and L.J.F.

## DECLARATION OF INTERESTS

The authors declare no competing interests.

Received: January 4, 2021

Revised: April 5, 2021

Accepted: June 1, 2021

Published: July 1, 2021

## REFERENCES

- Alfarano, C., Andrade, C.E., Anthony, K., Bahroos, N., Bajec, M., Bantoft, K., Betel, D., Bobechko, B., Boullier, K., Burgess, E., et al. (2005). The Biomolecular Interaction Network Database and related tools 2005 update. *Nucleic Acids Res.* *33*, D418–D424.
- Baldwin, A.J., Walsh, P., Hansen, D.F., Hilton, G.R., Benesch, J.L.P., Sharpe, S., and Kay, L.E. (2012). Probing dynamic conformations of the high-molecular-weight  $\alpha$ B-crystallin heat shock protein ensemble by NMR spectroscopy. *J. Am. Chem. Soc.* *134*, 15343–15350.
- Ballouz, S., Weber, M., Pavlidis, P., and Gillis, J. (2017). EGAD: ultra-fast functional analysis of gene networks. *Bioinformatics* *33*, 612–614.
- Barshir, R., Shwartz, O., Smoly, I.Y., and Yeger-Lotem, E. (2014). Comparative analysis of human tissue interactomes reveals factors leading to tissue-specific manifestation of hereditary diseases. *PLoS Comput. Biol.* *10*, e1003632.
- Basha, O., Argov, C.M., Artzy, R., Zoabi, Y., Hekselman, I., Alfandari, L., Chalfi-Caspi, V., and Yeger-Lotem, E. (2020). Differential network analysis of multiple human tissue interactomes highlights tissue-selective processes and genetic disorder genes. *Bioinformatics* *36*, 2821–2828.
- Bastian, F.B., Roux, J., Niknejad, A., Comte, A., Fonseca Costa, S.S., Mendes de Farias, T., Moretti, S., Parmentier, G., Rech de Laval, V., Rosikiewicz, M., et al. (2021). The Bgee suite: integrated curated expression atlas and comparative transcriptomics in animals. *Nucleic Acids Res.* *49*, D831–D847.
- Batada, N.N., Hurst, L.D., and Tyers, M. (2006). Evolutionary and physiological importance of hub proteins. *PLoS Comput. Biol.* *2*, e88.
- Battle, A., Khan, Z., Wang, S.H., Mitrano, A., Ford, M.J., Pritchard, J.K., and Gilad, Y. (2015). Genomic variation. Impact of regulatory variation from RNA to protein. *Science* *347*, 664–667.
- Bludau, I., Heusel, M., Frank, M., Rosenberger, G., Hafen, R., Banaei-Esfahani, A., van Drogen, A., Collins, B.C., Gstaiger, M., and Aebersold, R. (2020). Complex-centric proteome profiling by SEC-SWATH-MS for the parallel detection of hundreds of protein complexes. *Nat. Protoc.* *15*, 2341–2386.
- Bossi, A., and Lehner, B. (2009). Tissue specificity and the human protein interaction network. *Mol. Syst. Biol.* *5*, 260.
- Buljan, M., Chalancon, G., Eustermann, S., Wagner, G.P., Fuxreiter, M., Bateman, A., and Babu, M.M. (2012). Tissue-specific splicing of disordered segments that embed binding motifs rewires protein interaction networks. *Mol. Cell* *46*, 871–883.
- Calderone, A., Castagnoli, L., and Cesareni, G. (2013). mentha: a resource for browsing integrated protein-interaction networks. *Nat. Methods* *10*, 690–691.
- Capra, J.A., Williams, A.G., and Pollard, K.S. (2012). ProteinHistorian: tools for the comparative analysis of eukaryote protein origin. *PLoS Comput. Biol.* *8*, e1002567.

- Carlyle, B.C., Kitchen, R.R., Kanyo, J.E., Voss, E.Z., Pletikos, M., Sousa, A.M.M., Lam, T.T., Gerstein, M.B., Sestan, N., and Nairn, A.C. (2017). A multi-regional proteomic survey of the postnatal human brain. *Nat. Neurosci.* *20*, 1787–1795.
- Celaj, A., Schlecht, U., Smith, J.D., Xu, W., Suresh, S., Miranda, M., Aparicio, A.M., Proctor, M., Davis, R.W., Roth, F.P., and St Onge, R.P. (2017). Quantitative analysis of protein interaction network dynamics in yeast. *Mol. Syst. Biol.* *13*, 934.
- Chaillou, T., Zhang, X., and McCarthy, J.J. (2016). Expression of Muscle-Specific Ribosomal Protein L3-Like Impairs Myotube Growth. *J. Cell. Physiol.* *231*, 1894–1902.
- Chick, J.M., Munger, S.C., Simecek, P., Huttlin, E.L., Choi, K., Gatti, D.M., Raghupathy, N., Svenson, K.L., Churchill, G.A., and Gygi, S.P. (2016). Defining the consequences of genetic variation on a proteome-wide scale. *Nature* *534*, 500–505.
- Collins, S.R., Miller, K.M., Maas, N.L., Roguev, A., Fillingham, J., Chu, C.S., Schuldiner, M., Gebbia, M., Recht, J., Shales, M., et al. (2007). Functional dissection of protein complexes involved in yeast chromosome biology using a genetic interaction map. *Nature* *446*, 806–810.
- Csardi, G., and Nepusz, T. (2006). The igraph software package for complex network research. *InterJournal Complex Systems* *1695*, 1–9.
- Dai, M., Wang, P., Boyd, A.D., Kostov, G., Athey, B., Jones, E.G., Bunney, W.E., Myers, R.M., Speed, T.P., Akil, H., et al. (2005). Evolving gene/transcript definitions significantly alter the interpretation of GeneChip data. *Nucleic Acids Res.* *33*, e175.
- Das, J., and Yu, H. (2012). HINT: High-quality protein interactomes and their applications in understanding human disease. *BMC Syst. Biol.* *6*, 92.
- Davey, N.E., Van Roey, K., Weatheritt, R.J., Toedt, G., Uyar, B., Altenberg, B., Budd, A., Diella, F., Dinkel, H., and Gibson, T.J. (2012). Attributes of short linear motifs. *Mol. Biosyst.* *8*, 268–281.
- de Lichtenberg, U., Jensen, L.J., Brunak, S., and Bork, P. (2005). Dynamic complex formation during the yeast cell cycle. *Science* *307*, 724–727.
- Dosztányi, Z., Csizmok, V., Tompa, P., and Simon, I. (2005). IUPred: web server for the prediction of intrinsically unstructured regions of proteins based on estimated energy content. *Bioinformatics* *21*, 3433–3434.
- Edwards, M., Zwolak, A., Schafer, D.A., Sept, D., Dominguez, R., and Cooper, J.A. (2014). Capping protein regulators fine-tune actin assembly dynamics. *Nat. Rev. Mol. Cell Biol.* *15*, 677–689.
- Ellis, J.D., Barrios-Rodiles, M., Colak, R., Irimia, M., Kim, T., Calarco, J.A., Wang, X., Pan, Q., O'Hanlon, D., Kim, P.M., et al. (2012). Tissue-specific alternative splicing remodels protein-protein interaction networks. *Mol. Cell* *46*, 884–892.
- Enright, A.J., Van Dongen, S., and Ouzounis, C.A. (2002). An efficient algorithm for large-scale detection of protein families. *Nucleic Acids Res.* *30*, 1575–1584.
- Eyers, C.E., McNeill, H., Knebel, A., Morrice, N., Arthur, S.J.C., Cuenda, A., and Cohen, P. (2005). The phosphorylation of CapZ-interacting protein (CapZIP) by stress-activated protein kinases triggers its dissociation from CapZ. *Biochem. J.* *389*, 127–135.
- Floyd, B.J., Wilkerson, E.M., Veling, M.T., Minogue, C.E., Xia, C., Beebe, E.T., Wrobel, R.L., Cho, H., Kremer, L.S., Alston, C.L., et al. (2016). Mitochondrial protein interaction mapping identifies regulators of respiratory chain function. *Mol. Cell* *63*, 621–632.
- Fortelny, N., Butler, G.S., Overall, C.M., and Pavlidis, P. (2017). Protease-Inhibitor Interaction Predictions: Lessons on the Complexity of Protein-Protein Interactions. *Mol. Cell. Proteomics* *16*, 1038–1051.
- Fraser, H.B., Hirsh, A.E., Steinmetz, L.M., Scharfe, C., and Feldman, M.W. (2002). Evolutionary rate in the protein interaction network. *Science* *296*, 750–752.
- Geiger, T., Wehner, A., Schaab, C., Cox, J., and Mann, M. (2012). Comparative proteomic analysis of eleven common cell lines reveals ubiquitous but varying expression of most proteins. *Mol. Cell. Proteomics* *11*, M111.014050.
- Geiger, T., Velic, A., Macek, B., Lundberg, E., Kampf, C., Nagaraj, N., Uhlen, M., Cox, J., and Mann, M. (2013). Initial quantitative proteomic map of 28 mouse tissues using the SILAC mouse. *Mol. Cell. Proteomics* *12*, 1709–1722.
- Geladaki, A., Kočevár Britovšek, N., Breckels, L.M., Smith, T.S., Vennard, O.L., Mulvey, C.M., Crook, O.M., Gatto, L., and Lilley, K.S. (2019). Combining LOPIT with differential ultracentrifugation for high-resolution spatial proteomics. *Nat. Commun.* *10*, 331.
- Giurgiu, M., Reinhard, J., Brauner, B., Dunger-Kaltenbach, I., Fobo, G., Frishman, G., Montrone, C., and Ruepp, A. (2019). CORUM: the comprehensive resource of mammalian protein complexes-2019. *Nucleic Acids Res.* *47* (D1), D559–D563.
- Greene, C.S., Krishnan, A., Wong, A.K., Ricciotti, E., Zelaya, R.A., Himmelstein, D.S., Zhang, R., Hartmann, B.M., Zaslavsky, E., Sealfon, S.C., et al. (2015). Understanding multicellular function and disease with human tissue-specific networks. *Nat. Genet.* *47*, 569–576.
- Gsponer, J., Futschik, M.E., Teichmann, S.A., and Babu, M.M. (2008). Tight regulation of unstructured proteins: from transcript synthesis to protein degradation. *Science* *322*, 1365–1368.
- Guo, T., Kouvonen, P., Koh, C.C., Gillet, L.C., Wolski, W.E., Röst, H.L., Rosenberger, G., Collins, B.C., Blum, L.C., Gillesen, S., et al. (2015). Rapid mass spectrometric conversion of tissue biopsy samples into permanent quantitative digital proteome maps. *Nat. Med.* *21*, 407–413.
- Guruharsha, K.G., Rual, J.-F., Zhai, B., Mintseris, J., Vaidya, P., Vaidya, N., Beekman, C., Wong, C., Rhee, D.Y., Cenaj, O., et al. (2011). A protein complex network of *Drosophila melanogaster*. *Cell* *147*, 690–703.
- Havugimana, P.C., Hart, G.T., Nepusz, T., Yang, H., Turinsky, A.L., Li, Z., Wang, P.I., Boutz, D.R., Fong, V., Phanse, S., et al. (2012). A census of human soluble protein complexes. *Cell* *150*, 1068–1081.
- Hein, M.Y., Hubner, N.C., Poser, I., Cox, J., Nagaraj, N., Toyoda, Y., Gak, I.A., Weisswange, I., Mansfeld, J., Buchholz, F., et al. (2015). A human interactome in three quantitative dimensions organized by stoichiometries and abundances. *Cell* *163*, 712–723.
- Hekselman, I., and Yeger-Lotem, E. (2020). Mechanisms of tissue and cell-type specificity in heritable traits and diseases. *Nat. Rev. Genet.* *21*, 137–150.
- Heusel, M., Bludau, I., Rosenberger, G., Hafen, R., Frank, M., Banaei-Esfahani, A., van Droogen, A., Collins, B.C., Gstaiger, M., and Aebersold, R. (2019). Complex-centric proteome profiling by SEC-SWATH-MS. *Mol. Syst. Biol.* *15*, e8438.
- Heusel, M., Frank, M., Köhler, M., Amon, S., Frommelt, F., Rosenberger, G., Bludau, I., Aulakh, S., Linder, M.I., Liu, Y., et al. (2020). A Global Screen for Assembly State Changes of the Mitotic Proteome by SEC-SWATH-MS. *Cell Syst.* *10*, 133–155.
- Hubbell, E., Liu, W.-M., and Mei, R. (2002). Robust estimators for expression analysis. *Bioinformatics* *18*, 1585–1592.
- Hultqvist, G., Åberg, E., Camilloni, C., Sundell, G.N., Andersson, E., Dogan, J., Chi, C.N., Vendruscolo, M., and Jemth, P. (2017). Emergence and evolution of an interaction between intrinsically disordered proteins. *eLife* *6*. Published online April 11, 2017. <https://doi.org/10.7554/eLife.16059>.
- Huntley, R.P., Sawford, T., Mutowo-Muullenet, P., Shypitsyna, A., Bonilla, C., Martin, M.J., and O'Donovan, C. (2015). The GOA database: gene Ontology annotation updates for 2015. *Nucleic Acids Res.* *43*, D1057–D1063.
- Hurvich, C.M., and Tsai, C.-L. (1989). Regression and time series model selection in small samples. *Biometrika* *76*, 297–307.
- Huttlin, E.L., Jedrychowski, M.P., Elias, J.E., Goswami, T., Rad, R., Beausoleil, S.A., Villén, J., Haas, W., Sowa, M.E., and Gygi, S.P. (2010). A tissue-specific atlas of mouse protein phosphorylation and expression. *Cell* *143*, 1174–1189.
- Huttlin, E.L., Ting, L., Bruckner, R.J., Gebreab, F., Gygi, M.P., Szpyt, J., Tam, S., Zarraga, G., Colby, G., Baltier, K., et al. (2015). The bioplex network: A systematic exploration of the human interactome. *Cell* *162*, 425–440.
- Huttlin, E.L., Bruckner, R.J., Paulo, J.A., Cannon, J.R., Ting, L., Baltier, K., Colby, G., Gebreab, F., Gygi, M.P., Parzen, H., et al. (2017). Architecture of the human interactome defines protein communities and disease networks. *Nature* *545*, 505–509.

- Huttlin, E.L., Bruckner, R.J., Navarrete-Perea, J., Cannon, J.R., Baltier, K., Gebreab, F., Gygi, M.P., Thornock, A., Zárraga, G., Tam, S., et al. (2020). Dual Proteome-scale Networks Reveal Cell-specific Remodeling of the Human Interactome. *Cell*. Published online May 6, 2021. <https://doi.org/10.1016/j.cell.2021.04.011>.
- Iakoucheva, L.M., Radivojac, P., Brown, C.J., O'Connor, T.R., Sikes, J.G., Obradovic, Z., and Dunker, A.K. (2004). The importance of intrinsic disorder for protein phosphorylation. *Nucleic Acids Res.* *32*, 1037–1049.
- Jäger, S., Cimermancic, P., Gulbahce, N., Johnson, J.R., McGovern, K.E., Clarke, S.C., Shales, M., Mercenne, G., Pache, L., Li, K., et al. (2011). Global landscape of HIV-human protein complexes. *Nature* *481*, 365–370.
- Jeong, H., Mason, S.P., Barabási, A.L., and Oltvai, Z.N. (2001). Lethality and centrality in protein networks. *Nature* *411*, 41–42.
- Kerr, C.H., Skinnider, M.A., Andrews, D.D.T., Madero, A.M., Chan, Q.W.T., Stacey, R.G., Stoynov, N., Jan, E., and Foster, L.J. (2020). Dynamic rewiring of the human interactome by interferon signaling. *Genome Biol.* *21*, 140.
- Khan, Z., Ford, M.J., Cusanovich, D.A., Mitrano, A., Pritchard, J.K., and Gilad, Y. (2013). Primate transcript and protein expression levels evolve under compensatory selection pressures. *Science* *342*, 1100–1104.
- Kitsak, M., Sharma, A., Menche, J., Guney, E., Ghiassian, S.D., Loscalzo, J., and Barabási, A.-L. (2016). Tissue specificity of human disease module. *Sci. Rep.* *6*, 35241.
- Kolesnikov, N., Hastings, E., Keays, M., Melnichuk, O., Tang, Y.A., Williams, E., Dylag, M., Kurbatova, N., Brandizi, M., Burdett, T., et al. (2015). ArrayExpress update—simplifying data submissions. *Nucleic Acids Res.* *43*, D1113–D1116.
- Kotlyar, M., Pastrello, C., Pivetta, F., Lo Sardo, A., Cumbaa, C., Li, H., Nararian, T., Niu, Y., Ding, Z., Vafaee, F., et al. (2015). In silico prediction of physical protein interactions and characterization of interactome orphans. *Nat. Methods* *12*, 79–84.
- Kotlyar, M., Pastrello, C., Sheahan, N., and Jurisica, I. (2016). Integrated interactions database: tissue-specific view of the human and model organism interactomes. *Nucleic Acids Res.* *44* (D1), D536–D541.
- Kristensen, A.R., Gsponer, J., and Foster, L.J. (2012). A high-throughput approach for measuring temporal changes in the interactome. *Nat. Methods* *9*, 907–909.
- Krüger, M., Moser, M., Ussar, S., Thievensen, I., Luber, C.A., Forner, F., Schmidt, S., Zanivan, S., Fässler, R., and Mann, M. (2008). SILAC mouse for quantitative proteomics uncovers kindlin-3 as an essential factor for red blood cell function. *Cell* *134*, 353–364.
- Kühner, S., van Noort, V., Betts, M.J., Leo-Macias, A., Batisse, C., Rode, M., Yamada, T., Maier, T., Bader, S., Beltran-Alvarez, P., et al. (2009). Proteome organization in a genome-reduced bacterium. *Science* *326*, 1235–1240.
- Kuipers, H.F., Yoon, J., van Horssen, J., Han, M.H., Bollyky, P.L., Palmer, T.D., and Steinman, L. (2017). Phosphorylation of  $\alpha$ B-crystallin supports reactive astrogliosis in demyelination. *Proc. Natl. Acad. Sci. USA* *114*, E1745–E1754.
- Kundaje, A., Meuleman, W., Ernst, J., Bilenky, M., Yen, A., Heravi-Moussavi, A., Kheradpour, P., Zhang, Z., Wang, J., Ziller, M.J., et al.; Roadmap Epigenomics Consortium (2015). Integrative analysis of 111 reference human epigenomes. *Nature* *518*, 317–330.
- Kustatscher, G., Grabowski, P., Schrader, T.A., Passmore, J.B., Schrader, M., and Rappsilber, J. (2019). Co-regulation map of the human proteome enables identification of protein functions. *Nat. Biotechnol.* *37*, 1361–1371.
- Lage, K., Hansen, N.T., Karlberg, E.O., Eklund, A.C., Roque, F.S., Donahoe, P.K., Szallasi, Z., Jensen, T.S., and Brunak, S. (2008). A large-scale analysis of tissue-specific pathology and gene expression of human disease genes and complexes. *Proc. Natl. Acad. Sci. USA* *105*, 20870–20875.
- Lapek, J.D., Jr., Greninger, P., Morris, R., Amzallag, A., Pruteanu-Malinici, I., Benes, C.H., and Haas, W. (2017). Detection of dysregulated protein-association networks by high-throughput proteomics predicts cancer vulnerabilities. *Nat. Biotechnol.* *35*, 983–989.
- Leek, J.T., Johnson, W.E., Parker, H.S., Jaffe, A.E., and Storey, J.D. (2012). The sva package for removing batch effects and other unwanted variation in high-throughput experiments. *Bioinformatics* *28*, 882–883.
- Li, T., Wernersson, R., Hansen, R.B., Horn, H., Mercer, J., Slodkowitz, G., Workman, C.T., Rigina, O., Rapacki, K., Stærfeldt, H.H., et al. (2017). A scored human protein-protein interaction network to catalyze genomic interpretation. *Nat. Methods* *14*, 61–64.
- Licata, L., Briganti, L., Peluso, D., Perfetto, L., Iannuccelli, M., Galeota, E., Sacco, F., Palma, A., Nardoza, A.P., Santonico, E., et al. (2012). MINT, the molecular interaction database: 2012 update. *Nucleic Acids Res.* *40*, D857–D861.
- Liu, Z., Li, Y., Han, L., Li, J., Liu, J., Zhao, Z., Nie, W., Liu, Y., and Wang, R. (2015). PDB-wide collection of binding data: current status of the PDBbind database. *Bioinformatics* *31*, 405–412.
- Liu, Z., Miller, D., Li, F., Liu, X., and Levy, S.F. (2020). A large accessory protein interactome is rewired across environments. *eLife* *9*. Published online September 14, 2020. <https://doi.org/10.7554/eLife.62365>.
- Luck, K., Kim, D.-K., Lambourne, L., Spirohn, K., Begg, B.E., Bian, W., Brignall, R., Cafarelli, T., Campos-Laborie, F.J., Charlotteaux, B., et al. (2020). A reference map of the human binary protein interactome. *Nature* *580*, 402–408.
- Magger, O., Waldman, Y.Y., Rupp, E., and Sharan, R. (2012). Enhancing the prioritization of disease-causing genes through tissue specific protein interaction networks. *PLoS Comput. Biol.* *8*, e1002690.
- Marbach, D., Lamparter, D., Quon, G., Kellis, M., Kutalik, Z., and Bergmann, S. (2016). Tissue-specific regulatory circuits reveal variable modular perturbations across complex diseases. *Nat. Methods* *13*, 366–370.
- Markmiller, S., Soltanieh, S., Server, K.L., Mak, R., Jin, W., Fang, M.Y., Luo, E.-C., Krach, F., Yang, D., Sen, A., et al. (2018). Context-Dependent and Disease-Specific Diversity in Protein Interactions within Stress Granules. *Cell* *172*, 590–604.
- Maslov, S., and Sneppen, K. (2002). Specificity and stability in topology of protein networks. *Science* *296*, 910–913.
- Matthews, L.R., Vaglio, P., Reboul, J., Ge, H., Davis, B.P., Garrels, J., Vincent, S., and Vidal, M. (2001). Identification of potential interaction networks using sequence-based searches for conserved protein-protein interactions or “interologs”. *Genome Res.* *11*, 2120–2126.
- McClatchy, D.B., Liao, L., Park, S.K., Venable, J.D., and Yates, J.R. (2007). Quantification of the synaptosomal proteome of the rat cerebellum during post-natal development. *Genome Res.* *17*, 1378–1388.
- McWhite, C.D., Papoulas, O., Drew, K., Cox, R.M., June, V., Dong, O.X., Kwon, T., Wan, C., Salmi, M.L., Roux, S.J., et al. (2020). A Pan-plant Protein Complex Map Reveals Deep Conservation and Novel Assemblies. *Cell* *181*, 460–474.
- Melé, M., Ferreira, P.G., Reverter, F., DeLuca, D.S., Monlong, J., Sammeth, M., Young, T.R., Goldmann, J.M., Pervouchine, D.D., Sullivan, T.J., et al.; GTEx Consortium (2015). Human genomics. The human transcriptome across tissues and individuals. *Science* *348*, 660–665.
- Menche, J., Sharma, A., Kitsak, M., Ghiassian, S.D., Vidal, M., Loscalzo, J., and Barabási, A.-L. (2015a). Disease networks. Uncovering disease-disease relationships through the incomplete interactome. *Science* *347*, 1257601.
- Menche, J., Sharma, A., Kitsak, M., Ghiassian, S.D., Vidal, M., Loscalzo, J., and Barabási, A.L. (2015b). Disease networks. Uncovering disease-disease relationships through the incomplete interactome. *Science* *347*, 1257601, 1257601.
- Mészáros, B., Simon, I., and Dosztányi, Z. (2009). Prediction of protein binding regions in disordered proteins. *PLoS Comput. Biol.* *5*, e1000376.
- O'Hagan, S., Wright Muelas, M., Day, P.J., Lundberg, E., and Kell, D.B. (2018). Genegini: assessment via the gini coefficient of reference “housekeeping” genes and diverse human transporter expression profiles. *Cell Syst.* *6*, 230–244.
- Oliver, S. (2000). Guilt-by-association goes global. *Nature* *403*, 601–603.
- Orchard, S., Ammari, M., Aranda, B., Breuza, L., Briganti, L., Broackes-Carter, F., Campbell, N.H., Chavali, G., Chen, C., del-Toro, N., et al. (2014). The

- MIntAct project—IntAct as a common curation platform for 11 molecular interaction databases. *Nucleic Acids Res.* **42**, D358–D363.
- Ori, A., Iskar, M., Buczak, K., Kastriitis, P., Parca, L., Andrés-Pons, A., Singer, S., Bork, P., and Beck, M. (2016). Spatiotemporal variation of mammalian protein complex stoichiometries. *Genome Biol.* **17**, 47.
- Orre, L.M., Vesterlund, M., Pan, Y., Arslan, T., Zhu, Y., Fernandez Woodbridge, A., Frings, O., Fredlund, E., and Lehtiö, J. (2019). SubCellBarCode: Proteome-wide Mapping of Protein Localization and Relocalization. *Mol. Cell* **73**, 166–182.
- Oughtred, R., Stark, C., Breitkreutz, B.-J., Rust, J., Boucher, L., Chang, C., Kolas, N., O'Donnell, L., Leung, G., McAdam, R., et al. (2019). The BioGRID interaction database: 2019 update. *Nucleic Acids Res.* **47** (D1), D529–D541.
- Pankow, S., Bamberger, C., Calzolari, D., Martínez-Bartolomé, S., Lavallée-Adam, M., Balch, W.E., and Yates, J.R., 3rd. (2015).  $\Delta F508$  CFTR interactome remodelling promotes rescue of cystic fibrosis. *Nature* **528**, 510–516.
- Parker, B.L., Calkin, A.C., Seldin, M.M., Keating, M.F., Tarling, E.J., Yang, P., Moody, S.C., Liu, Y., Zereturk, E.J., Needham, E.J., et al. (2019). An integrative systems genetic analysis of mammalian lipid metabolism. *Nature* **567**, 187–193.
- Pellegrini, M., Marcotte, E.M., Thompson, M.J., Eisenberg, D., and Yeates, T.O. (1999). Assigning protein functions by comparative genome analysis: protein phylogenetic profiles. *Proc. Natl. Acad. Sci. USA* **96**, 4285–4288.
- Pierson, E., Koller, D., Battle, A., Mostafavi, S., Ardlie, K.G., Getz, G., Wright, F.A., Kellis, M., Volpi, S., and Dermitzakis, E.T.; GTEx Consortium (2015). Sharing and Specificity of Co-expression Networks across 35 Human Tissues. *PLoS Comput. Biol.* **11**, e1004220.
- Ramilowski, J.A., Goldberg, T., Harshbarger, J., Kloppmann, E., Lizio, M., Sataogom, V.P., Itoh, M., Kawaji, H., Carninci, P., Rost, B., and Forrest, A.R. (2015). A draft network of ligand-receptor-mediated multicellular signalling in human. *Nat. Commun.* **6**, 7866.
- Rappsilber, J., Mann, M., and Ishihama, Y. (2007). Protocol for micro-purification, enrichment, pre-fractionation and storage of peptides for proteomics using StageTips. *Nat. Protoc.* **2**, 1896–1906.
- Ray, J., Pinar, A., and Seshadhri, C. (2012). Are We There Yet? When to Stop a Markov Chain while Generating Random Graphs. In *Algorithms and Models for the Web Graph*, A. Bonato and J. Janssen, eds. (Springer), pp. 153–164.
- Razick, S., Magklaras, G., and Donaldson, I.M. (2008). iRefIndex: a consolidated protein interaction database with provenance. *BMC Bioinformatics* **9**, 405.
- Riniker, S., Fechner, N., and Landrum, G.A. (2013). Heterogeneous classifier fusion for ligand-based virtual screening: or, how decision making by committee can be a good thing. *J. Chem. Inf. Model.* **53**, 2829–2836.
- Rogers, L.D., Fang, Y., and Foster, L.J. (2010). An integrated global strategy for cell lysis, fractionation, enrichment and mass spectrometric analysis of phosphorylated peptides. *Mol. Biosyst.* **6**, 822–829.
- Rolland, T., Taşan, M., Charlotteaux, B., Pevzner, S.J., Zhong, Q., Sahni, N., Yi, S., Lemmens, I., Fontanillo, C., Mosca, R., et al. (2014). A proteome-scale map of the human interactome network. *Cell* **159**, 1212–1226.
- Romanov, N., Kuhn, M., Aebersold, R., Ori, A., Beck, M., and Bork, P. (2019). Disentangling genetic and environmental effects on the proteotypes of individuals. *Cell* **177**, 1308–1318.
- Romero, P.R., Zaidi, S., Fang, Y.Y., Uversky, V.N., Radivojac, P., Oldfield, C.J., Cortese, M.S., Sickmeier, M., LeGall, T., Obradovic, Z., and Dunker, A.K. (2006). Alternative splicing in concert with protein intrinsic disorder enables increased functional diversity in multicellular organisms. *Proc. Natl. Acad. Sci. USA* **103**, 8390–8395.
- Rosenberger, G., Heusel, M., Bludau, I., Collins, B.C., Martelli, C., Williams, E.G., Xue, P., Liu, Y., Aebersold, R., and Califano, A. (2020). SECAT: Quantifying Protein Complex Dynamics across Cell States by Network-Centric Analysis of SEC-SWATH-MS Profiles. *Cell Syst.* **11**, 589–607.
- Saha, A., Kim, Y., Gewirtz, A.D.H., Jo, B., Gao, C., McDowell, I.C., Engelhardt, B.E., and Battle, A.; GTEx Consortium (2017). Co-expression networks reveal the tissue-specific regulation of transcription and splicing. *Genome Res.* **27**, 1843–1858.
- Sahni, N., Yi, S., Taipale, M., Fuxman Bass, J.I., Coulombe-Huntington, J., Yang, F., Peng, J., Weile, J., Karras, G.I., Wang, Y., et al. (2015). Widespread macromolecular interaction perturbations in human genetic disorders. *Cell* **161**, 647–660.
- Salwinski, L., Miller, C.S., Smith, A.J., Pettit, F.K., Bowie, J.U., and Eisenberg, D. (2004). The Database of Interacting Proteins: 2004 update. *Nucleic Acids Res.* **32**, D449–D451.
- Sarkans, U., Gostev, M., Athar, A., Behrangi, E., Melnichuk, O., Ali, A., Minquet, J., Rada, J.C., Snow, C., Tikhonov, A., et al. (2018). The BioStudies database—one stop shop for all data supporting a life sciences study. *Nucleic Acids Res.* **46** (D1), D1266–D1270.
- Schwahnhauser, B., Busse, D., Li, N., Dittmar, G., Schuchhardt, J., Wolf, J., Chen, W., and Selbach, M. (2011). Global quantification of mammalian gene expression control. *Nature* **473**, 337–342.
- Schwikowski, B., Uetz, P., and Fields, S. (2000). A network of protein-protein interactions in yeast. *Nat. Biotechnol.* **18**, 1257–1261.
- Scott, N.E., Brown, L.M., Kristensen, A.R., and Foster, L.J. (2015). Development of a computational framework for the analysis of protein correlation profiling and spatial proteomics experiments. *J. Proteomics* **118**, 112–129.
- Scott, N.E., Rogers, L.D., Prudova, A., Brown, N.F., Fortelny, N., Overall, C.M., and Foster, L.J. (2017). Interactome disassembly during apoptosis occurs independent of caspase cleavage. *Mol. Syst. Biol.* **13**, 906.
- Shirasaki, D.I., Greiner, E.R., Al-Ramahi, I., Gray, M., Boontheung, P., Geschwind, D.H., Botas, J., Coppola, G., Horvath, S., Loo, J.A., and Yang, X.W. (2012). Network organization of the huntingtin proteomic interactome in mammalian brain. *Neuron* **75**, 41–57.
- Simonis, N., Rual, J.-F., Carvunis, A.-R., Tasan, M., Lemmens, I., Hirozane-Kishikawa, T., Hao, T., Sahalie, J.M., Venkatesan, K., Gebreab, F., et al. (2009). Empirically controlled mapping of the *Caenorhabditis elegans* protein-protein interactome network. *Nat. Methods* **6**, 47–54.
- Skinnider, M.A., Stacey, R.G., and Foster, L.J. (2018). Genomic data integration systematically biases interactome mapping. *PLoS Comput. Biol.* **14**, e1006474.
- Skinnider, M.A., Squair, J.W., and Foster, L.J. (2019). Evaluating measures of association for single-cell transcriptomics. *Nat. Methods* **16**, 381–386.
- Skinnider, M.A., Cai, C., Stacey, R.G., and Foster, L.J. (2021). PrInCE: an R/bioconductor package for protein-protein interaction network inference from co-fractionation mass spectrometry data. *Bioinformatics*, btab022.
- Smith, C.L., Blake, J.A., Kadin, J.A., Richardson, J.E., and Bult, C.J.; Mouse Genome Database Group (2018). Mouse Genome Database (MGD)—2018: knowledgebase for the laboratory mouse. *Nucleic Acids Res.* **46** (D1), D836–D842.
- Snider, J., Kotlyar, M., Saraon, P., Yao, Z., Jurisica, I., and Stagljar, I. (2015). Fundamentals of protein interaction network mapping. *Mol. Syst. Biol.* **11**, 848.
- Sonnhammer, E.L.L., and Östlund, G. (2015). InParanoid 8: orthology analysis between 273 proteomes, mostly eukaryotic. *Nucleic Acids Res.* **43**, D234–D239.
- Stacey, R.G., Skinnider, M.A., Scott, N.E., and Foster, L.J. (2017). A rapid and accurate approach for prediction of interactomes from co-elution data (PrInCE). *BMC Bioinformatics* **18**, 457.
- Stacey, R.G., Skinnider, M.A., Chik, J.H.L., and Foster, L.J. (2018). Context-specific interactions in literature-curated protein interaction databases. *BMC Genomics* **19**, 758.
- Thoroldsdottir, R.B., Sveinbjornsson, G., Sulem, P., Nielsen, J.B., Jonsson, S., Halldorsson, G.H., Melsted, P., Ivarsdottir, E.V., Davidsson, O.B., Kristjansson, R.P., et al. (2018). Coding variants in *RPL3L* and *MYZAP* increase risk of atrial fibrillation. *Commun. Biol.* **1**, 68.
- Tyanova, S., Temu, T., and Cox, J. (2016). The MaxQuant computational platform for mass spectrometry-based shotgun proteomics. *Nat. Protoc.* **11**, 2301–2319.

- Uhlén, M., Fagerberg, L., Hallström, B.M., Lindskog, C., Oksvold, P., Mardinoglu, A., Sivertsson, Å., Kampf, C., Sjöstedt, E., Asplund, A., et al. (2015). Proteomics. Tissue-based map of the human proteome. *Science* *347*, 1260419.
- Valášek, L.S., Zeman, J., Wagner, S., Beznosková, P., Pavlíková, Z., Mohammad, M.P., Hronová, V., Herrmannová, A., Hashem, Y., and Gunišová, S. (2017). Embraced by eIF3: structural and functional insights into the roles of eIF3 across the translation cycle. *Nucleic Acids Res.* *45*, 10948–10968.
- van Heesch, S., Witte, F., Schneider-Lunitz, V., Schulz, J.F., Adami, E., Faber, A.B., Kirchner, M., Maatz, H., Blachut, S., Sandmann, C.-L., et al. (2019). The translational landscape of the human heart. *Cell* *178*, 242–260.
- van Leeuwen, J., Pons, C., Mellor, J.C., Yamaguchi, T.N., Friesen, H., Koschwanetz, J., Ušaj, M.M., Pechlaner, M., Takar, M., Ušaj, M., et al. (2016). Exploring genetic suppression interactions on a global scale. *Science* *354*, aag0839.
- Vandenbon, A., Dinh, V.H., Mikami, N., Kitagawa, Y., Teraguchi, S., Ohkura, N., and Sakaguchi, S. (2016). Immuno-Navigator, a batch-corrected coexpression database, reveals cell type-specific gene networks in the immune system. *Proc. Natl. Acad. Sci. USA* *113*, E2393–E2402.
- Vidal, M., Cusick, M.E., and Barabási, A.-L. (2011). Interactome networks and human disease. *Cell* *144*, 986–998.
- Vizcaino, J.A., Deutsch, E.W., Wang, R., Csordas, A., Reisinger, F., Rios, D., Dianes, J.A., Sun, Z., Farrah, T., Bandeira, N., et al. (2014). ProteomeXchange provides globally coordinated proteomics data submission and dissemination. *Nat. Biotechnol.* *32*, 223–226.
- Vizcaino, J.A., Csordas, A., del-Toro, N., Dianes, J.A., Griss, J., Lavidas, I., Mayer, G., Perez-Riverol, Y., Reisinger, F., Trent, T., et al. (2016). 2016 update of the PRIDE database and its related tools. *Nucleic Acids Res.* *44* (D1), D447–D456.
- Voineagu, I., Wang, X., Johnston, P., Lowe, J.K., Tian, Y., Horvath, S., Mill, J., Cantor, R.M., Blencowe, B.J., and Geschwind, D.H. (2011). Transcriptomic analysis of autistic brain reveals convergent molecular pathology. *Nature* *474*, 380–384.
- Wan, C., Borgeson, B., Phanse, S., Tu, F., Drew, K., Clark, G., Xiong, X., Kagan, O., Kwan, J., Bezginov, A., et al. (2015). Panorama of ancient metazoan macromolecular complexes. *Nature* *525*, 339–344.
- Wang, S., Watanabe, T., Noritake, J., Fukata, M., Yoshimura, T., Itoh, N., Harada, T., Nakagawa, M., Matsuura, Y., Arimura, N., and Kaibuchi, K. (2007). IQ-GAP3, a novel effector of Rac1 and Cdc42, regulates neurite outgrowth. *J. Cell Sci.* *120*, 567–577.
- Wang, X., Wei, X., Thijssen, B., Das, J., Lipkin, S.M., and Yu, H. (2012). Three-dimensional reconstruction of protein networks provides insight into human genetic disease. *Nat. Biotechnol.* *30*, 159–164.
- Ward, J.J., Sodhi, J.S., McGuffin, L.J., Buxton, B.F., and Jones, D.T. (2004). Prediction and functional analysis of native disorder in proteins from the three kingdoms of life. *J. Mol. Biol.* *337*, 635–645.
- Wu, L., Candille, S.I., Choi, Y., Xie, D., Jiang, L., Li-Pook-Than, J., Tang, H., and Snyder, M. (2013). Variation and genetic control of protein abundance in humans. *Nature* *499*, 79–82.
- Yan, K.-K., Wang, D., Sethi, A., Muir, P., Kitchen, R., Cheng, C., and Gerstein, M. (2016). Cross-Disciplinary Network Comparison: Matchmaking Between Hairballs. *Cell Syst.* *2*, 147–157.
- Yu, H., Luscombe, N.M., Lu, H.X., Zhu, X., Xia, Y., Han, J.-D.J., Bertin, N., Chung, S., Vidal, M., and Gerstein, M. (2004). Annotation transfer between genomes: protein-protein interologs and protein-DNA regulogs. *Genome Res.* *14*, 1107–1118.
- Zanivan, S., Krueger, M., and Mann, M. (2012). In vivo quantitative proteomics: the SILAC mouse. *Methods Mol. Biol.* *757*, 435–450.
- Zhang, L., and Li, W.-H. (2004). Mammalian housekeeping genes evolve more slowly than tissue-specific genes. *Mol. Biol. Evol.* *21*, 236–239.
- Zhang, B., Gaiteri, C., Bodea, L.-G., Wang, Z., McElwee, J., Podtelezchnikov, A.A., Zhang, C., Xie, T., Tran, L., Dobrin, R., et al. (2013). Integrated systems approach identifies genetic nodes and networks in late-onset Alzheimer's disease. *Cell* *153*, 707–720.
- Zhou, Q., Liu, M., Xia, X., Gong, T., Feng, J., Liu, W., Liu, Y., Zhen, B., Wang, Y., Ding, C., and Qin, J. (2017). A mouse tissue transcription factor atlas. *Nat. Commun.* *8*, 15089.

## STAR★METHODS

### KEY RESOURCES TABLE

REAGENT or RESOURCE	SOURCE	IDENTIFIER
<b>Antibodies</b>		
Mouse monoclonal anti-Talin	Santa Cruz	Sc-365875
<b>Biological samples</b>		
C57BL/6 mice F2 Lys-6 labeled brain, heart, thymus, liver, kidney, skeletal muscle, lung	Produced in house from C57BL/6 mice F0, Charles River Laboratories (Lys-6 diet)	N/A
C57BL/6 mice F2 Lys-0 labeled brain, heart, thymus, liver, kidney, skeletal muscle, lung	Produced in house from C57BL/6 mice F0, Charles River Laboratories (unlabelled diet)	N/A
C57BL/6 mice F1 (lung, skeletal muscle, kidney, liver, thymus, heart, brain) for immunoprecipitation validation	Produced in house from C57BL/6 mice F0, Charles River Laboratories (unlabelled diet)	N/A
<b>Chemicals, peptides, and recombinant proteins</b>		
MouseExpress L-LYSINE (13C6, 99%) IRRADIATED MOUSE FEED 8G/KG OF L-LYSINE 13C6	Cambridge Isotope Laboratories, Inc.	MF-LYS-C-LOW-IR
MouseExpress UNLABELED MOUSE FEED IRRADIATED	Cambridge Isotope Laboratories, Inc.	MF-UNLABELED-LOW-IR
Halt Protease and Phosphatase Inhibitor Cocktail	Thermo Scientific, San Jose CA	78442
Lysyl Endopeptidase (Lys-C)	Wako Pure Chemical Industries, Ltd., Japan	125-05061
<b>Deposited data</b>		
Raw mass spectrometry proteomics data	This paper	ProteomeXchange Consortium: PXD007288 and PXD022309
Processed chromatograms	This paper	EMBL–EBI BioStudies database: S-BSST152
<b>Experimental models: Organisms/strains</b>		
C57BL/6 mice F0	Charles River Laboratories	Strain code 027
<b>Software and algorithms</b>		
MaxQuant	<a href="https://www.maxquant.org/">https://www.maxquant.org/</a>	Versions 1.5.3.30, 1.5.5.1, 1.6.5.0
PrInCE	<a href="https://github.com/fosterlab/PrInCE">https://github.com/fosterlab/PrInCE</a>	Version 1.5.0
<b>Other</b>		
Vivaspin® 2 ultrafiltration centrifugal concentrators (100,000 Da MWCO)	Sartorius Stedim, Goettingen, Germany	VS0241
BioSep-4000 SEC column (300 × 7.8 mm)	Phenomenex	00H-2147-K0
UniFilter 800 96-well Filtration microplates	GE Healthcare Life Sciences	7700-2803
5.0-µm Aqua C18 packing material	Phenomenex	00F-4299-E0
ReproSil-Pur C18 AQ 1.9 µm	Dr. Maisch, Ammerbuch-Entringen, Germany	R119 aq.0001

### RESOURCE AVAILABILITY

#### Lead contact

Further information and requests for resources and reagents should be directed to and will be fulfilled by the Lead Contact, Leonard Foster ([foster@msl.ubc.ca](mailto:foster@msl.ubc.ca)).

#### Materials availability

This study did not generate new unique reagents.

### Data and code availability

The mass spectrometry proteomics data have been deposited to the ProteomeXchange Consortium (Vizcaíno et al., 2014) via the PRIDE partner repository (Vizcaíno et al., 2016) with the dataset identifiers PXD007288 and PXD022309. In addition, processed chromatograms for each tissue have been deposited to the EMBL-EBI BioStudies database (Sarkans et al., 2018), with accession S-BSST152.

### EXPERIMENTAL MODEL AND SUBJECT DETAILS

Protocols for the generation of SILAM labeled and unlabelled tissues were approved by the University of British Columbia Animal Care Committee in accordance with international guidelines (protocol number: A13-0094). SILAM colonies and unlabelled littermate controls were generated according to the approach of Krüger et al. (Krüger et al., 2008; Zanivan et al., 2012). Briefly, two sets of female and male littermate C57BL/6 mice (Charles River Laboratories) aged 8 weeks were segregated into separate cages and female mice fed either a SILAC chow diet (8 g  $^{13}\text{C}_6$ -Lysine/kg, Cambridge Isotope Laboratories, Andover, MA) or unlabelled matched chow diet differing only in the incorporation of  $^{13}\text{C}_6$ -Lysine. After 10 weeks of SILAC feeding, male mice were introduced to F0 SILAM females to allow mating. The resulting F1 SILAM mice were allowed to develop to 8 weeks and were subjected to another round of mating to generate F2 SILAM mice. F2 SILAM mice were allowed to develop to 8 weeks prior to tissue isolation and protein complex extraction. In parallel to the generation of SILAM mice, unlabelled mice were derived from littermates of the F0 SILAM breed and allowed to develop to 8 weeks. Tissues were harvested from 8-week old C57BL/6 male mice. Animals were housed with littermates of the same sex, up to 4 per cage, with environmental enrichment according to the University of British Columbia Animal Care requirements.

### METHOD DETAILS

#### SILAM incorporation monitoring

SILAM incorporation rates were monitored in female mice during the generation of F1 and F2 litters. For blood sample collection, mice were anesthetized with isoflurane and  $\sim 20$   $\mu\text{L}$  of blood was collected by tail snipping every month during SILAM feeding. To measure isotope incorporation, the medulla oblongata was collected during animal termination of F0, F1 and F2 mice. Blood and medulla oblongata samples for SILAM incorporation analysis were snap frozen in liquid nitrogen and stored at  $-80^\circ\text{C}$ . Samples were boiled in 1% sodium deoxycholate, digested, and quantified as described below.

#### Tissue harvesting

Mice were terminally anesthetized with isoflurane and after the loss of corneal reflexes moved to a chilled surgical platform. To limit blood contamination within tissues and inhibit phosphatase and protease activity, the heart was exposed by Y-incision and mice perfused with 50 mL of ice-cold size exclusion chromatography (SEC) mobile phase [50 mM KCl, 50 mM  $\text{NaCH}_3\text{COO}$ , pH 7.2, containing 2x cOmplete protease inhibitor cocktail without EDTA (Roche) and 2x Halt protease and phosphatase inhibitor cocktail (Thermo Scientific, San Jose CA)]. Perfusate was introduced into the left ventricle by precising the ventricle wall with a needle while the right ventricle was cut to allow drainage. Upon complete blanching of the liver, the seven tissues of interest (heart, brain, thymus, liver, kidney, skeletal muscle, and lung) were removed, rinsed with ice-cold SEC buffer and placed into ice-cold SEC containing 2x protease inhibitor cocktail without EDTA and 2x protease and phosphatase inhibitor cocktail. Tissues were further cut into smaller pieces to enhance accessibility of inhibitors and placed on ice.

#### Preparation of cytoplasmic complexes

Complex preparation of dissected tissues and size exclusion chromatography were performed as described previously (Kristensen et al., 2012), with minor modifications. Briefly, tissues samples were lysed using a Dounce homogenizer with 200 strokes of a loose pestle followed by 200 strokes with a tight pestle. Lysates were ultracentrifuged at 100,000 relative centrifugal force (r.c.f.) for 15 min at  $4^\circ\text{C}$  to remove insoluble material and to partially deplete highly abundant ribosomes. Large molecular weight complexes were then concentrated using 100,000 Da molecular weight cut-off spin columns (Sartorius Stedim, Goettingen, Germany). Five milligrams of total filtered protein was then immediately loaded onto a chromatography system consisting of two  $300 \times 7.8$  mm BioSep-4000 Columns (Phenomenex, Torrance, CA) equilibrated with SEC mobile phase and separated into 80 fractions by a 1200 Series semi-preparative HPLC (Agilent Technologies, Santa Clara, CA) at a flow rate of 0.5 mL/min at  $8^\circ\text{C}$ . The HPLC consisted of a G1310A isocratic pump, G7725i manual injector, and G1364 fraction collector with a G1330 thermostat. Fractions 1 to 55 corresponded to molecular weights from 2 MDa to 100 KDa, as determined by the use of common SEC standards thyroglobulin, apoferritin and bovine serum albumin (Sigma-Aldrich). Each tissue was separated independently by SEC for both labeled and unlabelled samples. Fractions 1 to 55 from the seven heavy-labeled tissue preparations were pooled and served as an internal reference allowing the comparison between and across all samples. The pooled reference was spiked into each of the corresponding light fractions at a volume of 1:0.75 (light to heavy).

#### In-solution digestion

Individual PCP-SILAM samples were prepared using in-solution digestion as previously described (Rogers et al., 2010). Briefly, sodium deoxycholate was added to each fraction to a final concentration of 1.0% (w/v) and samples boiled for 5 min. Boiled samples

were allowed to cool to RT then reduced for 1 hour with 10 mM dithiothreitol (DTT) at room temperature. Samples were then alkylated for 1 h with 20 mM iodoacetamide (IAA) in the dark at room temperature and excess IAA quenched with 40mM DTT for 20 min. Two micrograms of Lys-C (Wako) was added to each fraction and samples were incubated overnight at 37°C with shaking. Samples were acidified to pH < 3 with acetic acid to precipitate deoxycholic acid, which was then removed by centrifugation at 16,000 r.c.f. for 20 min. To ensure the removal of particulate matter, peptide digests were further clarified using Unifilter 800 Whatman filter plates (GE Healthcare Life Sciences). The resulting peptide supernatant was purified using self-made Stop-and-go-extraction tips (Stage-Tips) (Rappsilber et al., 2007) composed of C18 Empore material (3M) packed into 200  $\mu$ L pipette tips. Prior to addition of the peptide solution, StageTips were conditioned with methanol, followed by 80% MeCN, 0.1% formic acid (Buffer B), then 0.1% formic acid (Buffer A). Peptide supernatants were loaded onto columns and washed with three bed volumes of Buffer A. Peptide samples were stored directly on stage tip at 4°C until required, when they were eluted with Buffer B directly into a HPLC autosampler plate and dried using a vacuum concentrator. An alternative in-solution digestion method was used for a subset of sample sets. For these, each fraction was denatured with 6 M urea / 2 M thiourea, reduced for 30 min with 10 mM DTT at room temperature, alkylated for 30 min with 20 mM IAA in the dark at room temperature. A mixture of 1.5  $\mu$ g of Lys-C, 4 mM DTT, and 50 mM ammonium bicarbonate was added to each fraction to dilute urea to 2 M and incubated overnight at room temperature with shaking. The peptides were purified with Stage Tips, eluted, and dried using a vacuum concentrator.

### Mass spectrometry

Prior to LC-MS/MS analysis, samples were resuspended in 15  $\mu$ L Buffer A. One of three LC-MS/MS was used: one subset was acquired using an EASY-nLC1000 system (Thermo Scientific) coupled to a Q-Exactive mass spectrometer (Thermo Scientific). Another subset used a Dionex Ultimate 3000 UHPLC (Thermo Scientific) coupled to a Q-Exactive plus mass spectrometer (Thermo Scientific). The final subset used an EASY-nLC1000 (Thermo Scientific) coupled to a quadrupole-time of flight mass spectrometer (Impact II; Bruker Daltonics). LC-MS/MS was accomplished using a two-column system in which samples were concentrated prior to separation on an in-house packed 2 cm long, 100  $\mu$ m inner diameter fused silica fritted trap column containing 5  $\mu$ m Aqua C18 beads (Phenomenex) and then separated using an in-house packed C18 analytical 75- $\mu$ m inner diameter column composed of 35 cm ReproSil-Pur C18 AQ 1.9  $\mu$ m (Dr. Maisch, Ammerbuch-Entringen, Germany) column with an integrated spray tip (6–8  $\mu$ m-diameter opening, pulled on a P-2000 laser puller from Sutter Instruments) that is held at 50°C by an in-house built column heater or a PepMap100 C18 20 mm x 75  $\mu$ m trap and a PepMap C18 500 mm x 75  $\mu$ m analytical column (Thermo Fisher Scientific). Samples were concentrated onto the trap for 5 min using 100% Buffer A at 5 L/min after which the gradient was altered from 100% Buffer A to 40% Buffer B over 180 min at 250 nL/min with the eluting peptides infused directly into the mass spectrometers via nESI. An alternative gradient was shortened to 150 min separation. The Q-Exactive and Q-Exactive Plus were operated in a data-dependent manner using Xcalibur (Thermo Scientific) with the top ten most intense multiply-charged ions above a 5% underfill ratio from MS1 scans (resolution 70,000; 350–2,000 m/z, AGC target of  $3 \times 10^6$ ) selected for HCD MS-MS events (resolution 17.5k AGC target of  $1 \times 10^6$  with a maximum injection time of 60 or 120 ms, NCE 28 with 20% stepping) with 25 s dynamic exclusion enabled. The Impact II was operated in a data-dependent auto-MS/MS mode with inactive focus fragmenting the 20 most abundant ions (one at the time at 18 Hz rate) after each full-range scan from m/z 200 to m/z 2000 at 5 Hz rate. The isolation window for MS/MS was between 2 and 3 units depending on the parent ion mass to charge ratio, and the collision energy ranged from 23 to 65 eV depending on ion mass and charge. Parent ions were then excluded from MS/MS for the next 0.4 min and reconsidered if their intensity increased more than five times. Singly charged ions were excluded from fragmentation.

### Co-immunoprecipitation

For talin immunoprecipitations, brain and liver tissues collected from 3 mice (B10, male, 10-week old), were rinsed in ice cold in size-exclusion chromatography (SEC) mobile phase (50 mM Tris, 50 mM KCl, 50 mM NaCH<sub>3</sub>COO, pH 7.2) including protease inhibitors without EDTA (Roche) and phosphatase inhibitors (1 mM sodium orthovanadate, 5 mM sodium pyrovanadate and 0.5 mM pervanadate) and placed on ice. Tissues (100–200 mg) were individually disrupted in a Dounce homogenizer (2 min, tight dounce) in 2 mL of ice-cold size-exclusion chromatography (SEC) mobile phase (50 mM Tris, 50 mM KCl, 50 mM NaCH<sub>3</sub>COO, pH 7.2) including protease inhibitors without EDTA (Roche) and phosphatase inhibitors (1 mM sodium orthovanadate, 5 mM sodium pyrovanadate and 0.5 mM pervanadate). The resulting lysates were clarified by centrifugation (15 min; 4°C; 16000 r.c.f.) and 1 mL of each supernatant was used for immunoprecipitation using C-9 mouse monoclonal talin antibody (sc-365875, Santa Cruz) following the manufacturer's protocol. Briefly, the lysates were pre-cleared for 30 min using mouse IgG and protein L-agarose (sc-2336, Santa Cruz), incubated for 30 min with 2 mg of primary antibody, followed by 30 min incubation with protein L-agarose. The bound beads were washed twice with ice-cold SEC buffer and the protein eluted by boiling with the Laemmli buffer. The resulting proteins were subjected to SDS-PAGE, in gel-digested, purified on STAGE tips and analyzed by mass spectrometry.

### Ribosome isolation

Tissues were harvested from two 10-week old C57BL/6 male mice and rinsed two times in PBS. Tissues were then minced using a scalpel and suspended in 3 mL of Ribosome Homogenization Buffer (50 mM Tris-HCl pH 7.5, 5 mM MgCl<sub>2</sub>, 25 mM KCl, 0.2 M sucrose). Tissue samples were homogenized for 1 min using a loose Dounce homogenizer followed by 2 min in a tight Dounce homogenizer. Lysates were clarified through centrifugation using a Sorvall Surespin 630 rotor at 20,000 r.c.f. for 10 min at 4°C. The crude

lysates were then layered over a sucrose cushion (50 mM Tris-HCl pH 7.5, 5 mM MgCl<sub>2</sub>, 25 mM KCl, 2 M sucrose) at a 1:1 (v/v) ratio. Subsequently, samples were ultracentrifuged at 100,000 r.c.f. for 24 h at 4°C. The resulting pellet was resuspended in Ribosome Homogenization Buffer. Protein concentration was determined via NanoDrop (Thermo Fisher). Equal amount of protein from each tissue sample was then denatured with 6M urea, reduced with 1 μg of DTT, alkylated with 2.5 μg of iodoacetamide, followed by adding four volumes of 50 mM NH<sub>4</sub>HCO<sub>3</sub> and subjected to trypsin digestion overnight at room temperature. Peptide samples were cleaned via STAGE tips and analyzed by LC-MS/MS. The raw data was searched using MaxQuant version 1.5.3.30 with variable modifications: acetylation (K), deamidation (NQ), and oxidation (M); fixed modifications: carbamidomethyl (C); and label-free quantitation with a minimum ratio count of 1. The resulting LFQ intensities were normalized to the median ribosomal protein intensity in each replicate.

## QUANTIFICATION AND STATISTICAL ANALYSIS

### Proteomic data analysis

MaxQuant (versions 1.5.5.1 and 1.6.5.0) (Tyanova et al., 2016) was used for identification and quantification of the resulting experiments. Database searching was carried out against the UniProt *Mus musculus* database (downloaded August 17, 2014; 49,235 entries), augmented with common contaminants, with the following search parameters: carbamidomethylation of cysteine as a fixed modification, oxidation of methionine, and acetylation of protein N-termini. The digestion mode was either semi-specific LysC or specific LysC with a maximum of two missed cleavages. A multiplicity of two was used, denoting the SILAM amino acid combinations (light lysine and heavy lysine respectively). The precursor mass tolerance was set to 7 parts-per-million (ppm) and MS/MS of 10 ppm, with a maximum false discovery rate of 1% set for protein identifications and peptide-spectrum matches, which was filtered to 1% at the peptide and protein level after peptide score correction. To enhance the identification of peptides between fractions and replicates, the match between runs option was enabled with a precursor match window set to 2 min and an alignment window of 10 min. Potential contaminants, reverse hits, and proteins identified only by modified peptides were removed. Protein groups were mapped to gene symbols, retaining only the chromatogram with the greatest number of non-missing observations in cases where multiple protein groups mapped to a single symbol. These steps yielded a matrix reflecting the abundance of 7,225 proteins across 770 SEC fractions.

To evaluate the accuracy of SILAM-based protein quantification, we compared the SILAM ratios to quantifications based on the MS1 intensities in the light channel only. We computed two measures of quantitative precision: the coefficient of variation between biological replicates for individual protein quantifications; and the rank correlations between biological replicates across entire protein chromatograms. Additionally, we compared the total number of proteins by either method through a downsampling analysis, drawing 100 random samples of between 1 and 770 SEC fractions and computing the total number of proteins quantified in each sample.

To evaluate the reproducibility of PCP-SILAM, we computed the Spearman correlations between each biological replicate from the same tissue, and compared these to correlations between biological replicates in published, cell-line-based PCP-SILAC data from three studies (Kerr et al., 2020; Scott et al., 2015, 2017), collectively representing a total of 26 replicate pairs. We additionally performed hierarchical clustering of all fourteen PCP-SILAM replicates, using the Spearman correlation as the similarity measure.

To evaluate the statistical power of PCP-SILAM to resolve known protein complexes, we reproduced a receiver operating characteristic (ROC) analysis (Romanov et al., 2019) of large-scale shotgun proteomics datasets (Battle et al., 2015; Carlyle et al., 2017; Chick et al., 2016; Geiger et al., 2012, 2013; Guo et al., 2015; Khan et al., 2013; Kustatscher et al., 2019; Parker et al., 2019; Wu et al., 2013), additionally comparing to matched transcriptomic (Battle et al., 2015; Carlyle et al., 2017; Chick et al., 2016; van Heesch et al., 2019; Khan et al., 2013), and translational (Battle et al., 2015; van Heesch et al., 2019) data when possible. Briefly, the Pearson correlation was calculated between each gene or protein pair in every dataset, and pairs quantified in fewer than ten overlapping samples were filtered to mitigate the impact of spurious correlations. Then, gene or protein pairs were labeled as true positives and true negatives based on the dataset of protein complexes manually curated by (Ori et al., 2016), calling intra-complex pairs as true positives and inter-complex pairs as true negatives. Finally, we used these labels to calculate the area under the receiver operating characteristic curve (AUC), using the 'AUC' R package. We additionally compared the AUC in *in vivo* PCP-SILAM data to *in vitro* data from four previous PCP-SILAC studies using the same procedure (Kerr et al., 2020; Scott et al., 2015, 2017; Stacey et al., 2018), observing no significant difference.

### Interactome network inference

PrInCE (Stacey et al., 2017), an open-source pipeline for co-fractionation mass spectrometry data analysis, was used to reconstruct high-confidence interactomes from PCP-SILAM profiles. PrInCE first performs basic data filtering and preprocessing, then applies a machine-learning approach to rank interactions, and returns as output a list of interactions at a given precision threshold. Briefly, single missing values are imputed as the mean of neighboring intensities, proteins detected in fewer than five fractions are filtered, and co-fractionation profiles are smoothed by a sliding average with a width of five fractions. Next, mixtures of one to five Gaussians are fitted to each profile, and model selection is performed using the bias-corrected Akaike information criterion (Hurvich and Tsai, 1989). Then, six measures of distance or similarity are calculated for each protein pair, each of which reflects the likelihood of a physical interaction between those two proteins based on their mass spectrometric profiles. These six features include the Pearson correlation coefficient (calculated separately for both the raw and smoothed chromatograms), as well as its *P* value in the raw chromatograms; the Euclidean

distance between chromatograms; the number of fractions separating the maximum values of each co-fractionation profile; and the distance between the closest pair of fitted Gaussians. Missing values in the feature matrix are imputed with the median, plus or minus a small amount of random noise, sampled from a normal distribution with a mean of zero and a standard deviation equal to 5% of the standard deviation of the relevant feature. A classifier is subsequently trained on a reference set of interactions in 10-fold cross-validation, taking pairs of proteins within the same complex as true positives and pairs of proteins in different complexes as true negatives, and predictions are made for the entire test set (and all proteins not found in any training set complex) during each fold of cross-validation. Protein pairs are then ranked as candidate interactions based on their median score across all ten cross-validation folds. PrInCE implements a number of classifiers for use in network inference; here, we used heterogeneous classifier fusion (Riniker et al., 2013), as implemented in the PrInCE Bioconductor package (Skinnider et al., 2021), to train an ensemble of classifiers, including naive Bayes, random forest, logistic regression, and support vector machine models, then aggregated predictions by taking the mean rank across all four classifiers. This strategy improves the robustness of the network inference procedure by down-weighting spurious protein pairs that are highly ranked only by a single model while up-weighting pairs that are ranked near the top by all classifiers (Skinnider et al., 2021).

The interaction score calculated for each protein pair is then converted to a measure of precision (or, equivalently, a false discovery rate) for each interaction by calculating the ratio of true positives to true positives and true negatives among interactions at that probability or higher. Finally, a list of interactions is output at a user-specified precision. We applied PrInCE to each of the two replicates in each tissue separately, then combined and re-scored interactions detected in either replicate by the application of Fisher's method to the false discovery rates of each interaction in either replicate. Only protein pairs co-eluting in at least five overlapping fractions were considered as potential interactors. Interactions detected within each tissue at 95% precision or higher (equivalent to a 5% false discovery rate) were retained for further analysis.

Like previous machine-learning approaches to network inference from co-fractionation mass spectrometry (Havugimana et al., 2012; Wan et al., 2015), PrInCE requires a resource of known protein complexes to train the classifier, such as those provided by the CORUM database (Giurgiu et al., 2019) or the manually curated dataset of Ori et al. Previously, however, we observed that several of these protein complexes may be degraded or disassembled under PCP assay conditions (Stacey et al., 2018). We found that using these protein complexes to train a classifier impairs the ability of that classifier to distinguish interacting and non-interacting protein pairs, as the complexes in question may display little statistical evidence of co-elution. However, we found that the accuracy of network inference could be substantially improved by using only a subset of CORUM protein complexes that had consistently co-eluted in previously published PCP studies to train the classifier (Stacey et al., 2018), and we therefore used that same subset in this study.

To evaluate the robustness of the inferred tissue interactomes to slight variations in the analysis workflow, we carried out a series of additional PrInCE analyses, varying the parameters used in network inference. These parameters varied included: (i) the minimum number of points required to retain (by default, PrInCE retains only chromatograms with at least five consecutive points, after imputing single missing values with the average of their neighbors); (ii) the minimum number of fractions in which two proteins were required to be jointly detected to be considered as potential interactors; (iii) the maximum number of Gaussian peaks with which each chromatogram was fit; (iv) the minimum  $r^2$  used to accept a fitted mixture of Gaussians; (v) the features used as input to the model, where each one of the features described above was held out from the input feature matrix in turn; (vi) the number of cross-validation folds performed; (vii) the total number of times the cross-validation procedure was repeated; (viii) the number of trees in the random forest classifier; and (ix) the classifiers used in the ensemble, where each of the three classifiers (naive Bayes, support vector machine, and random forest) was held out from the ensemble in turn. For each alternative set of parameters, we retained a matching number of interactions in each tissue, and calculated the proportion of interactions that were reproduced in that tissue after varying the PrInCE parameters. We also evaluated the inherent stochasticity in the cross-validation procedure itself by running PrInCE a second time with the default parameters and computing the overlap analogously, finding that between 98.3% and 99.2% of the interactions were reproduced in each tissue.

To evaluate the tissue specificity of the interactions, we analyzed the properties of the fitted Gaussians for each protein pair in tissues where an interaction was or was not assigned by PrInCE. We first extracted the peak shift, defined as the distance (in fractions) between the closest pair of fitted Gaussians for each potential interaction, and compared this distance between tissues in which the interaction was or was not detected by PrInCE. For proteins with a peak shift less than two fractions, we also calculated the stoichiometry of the interaction, defined as the ratio between the heights of the two Gaussians. We used the smaller Gaussian peak as the denominator to ensure all ratios were greater than or equal to 1. To assess the conservation of the interaction stoichiometry, we computed the standard deviation of this ratio across tissues in which the interaction was or was not detected by PrInCE. We evaluated the statistical significance of these differences using the Brunner-Munzel test.

### Comparison to published interactomes

Interaction data from the BioPlex (Huttlin et al., 2015), BioPlex 2 (Huttlin et al., 2017), HI-II-14 (Rolland et al., 2014), QUBIC (Hein et al., 2015), and HuRI (Luck et al., 2020) screens were downloaded from the supporting information of the respective publications and mapped to gene symbols. In addition, a master database of 82,602 experimentally detected mouse interactions was compiled by merging interactions from nine databases, including BIND (Alfarano et al., 2005) BioGRID (Oughtred et al., 2019), CORUM (Giurgiu et al., 2019), DIP (Salwinski et al., 2004), HINT (Das and Yu, 2012), IntAct (Orchard et al., 2014), iRefIndex (Razick et al., 2008), mentha

(Calderone et al., 2013), and MINT (Licata et al., 2012). Each interaction was associated with one or more publication(s) in which the interaction was reported; interactions without a traceable publication were assumed to be reported in a single publication. Identifiers were mapped to gene symbols, and self-interactions were removed. The master database was then partitioned into interactions reported in at least one, two, three, or four publications. Finally, manually curated protein complexes were obtained from Ori et al. (2016). This yielded a total of 17 interactome networks.

Due to the relatively small number of known interactions in mouse, we also evaluated the overlap between our PCP-SILAM interactomes and a larger resource of human interactions detected by small-scale experiments. Human interactions were obtained from the BioGRID database (Oughtred et al., 2019) and studies reporting more than 100 interactions were removed. We used this resource to compute the proportion of interactions in (i) the PCP-SILAM interactomes and (ii) the five human high-throughput screens listed above that had previously been detected by a small-scale study. We also obtained a set of human genetic interactions from BioGRID and used these to perform a similar analysis.

Human and mouse GO annotations were obtained from the UniProt-GOA (Huntley et al., 2015). Annotations with the evidence codes “IPI” (inferred from physical interaction), “IEA” (inferred from electronic annotation), or “ND” (no data), or the qualifier “NOT,” were removed.

For each network, we computed a series of indices that reflect the concordance of the network with other large-scale genomic datasets. First, we calculated the functional coherence of the network, using the EGAD R package (Ballouz et al., 2017), as previously described (Skinnider et al., 2018, 2019). In this analysis, each gene in the network is annotated with its known functions (that is, GO terms), and a subset of these labels is then randomly withheld. A simple neighbor-voting algorithm (Schwikowski et al., 2000) is then used to predict functions for the withheld proteins. That is, for each protein in the held-out set, a score is assigned for each GO term that reflects the proportion of that protein’s interacting partners annotated with the GO term of interest. The process is repeated in three-fold cross-validation, and the AUC is calculated for each GO term, thereby quantifying the accuracy of protein function predictions made based on the topology of the network alone. As an alternative measure of functional connectivity, we computed the graph assortativity of each GO term (Huttlin et al., 2020), which quantifies the tendency of proteins annotated to a particular GO term to interact with other proteins annotated to the same term, and observed similar results. In both cases, we discarded GO terms annotated to less than 20 or more than 200 proteins, in order to mitigate the impact of very specific or very broad GO terms on the results (Skinnider et al., 2018, 2019). Second, we computed the coexpression of each interacting protein pair, quantified using the Pearson correlation coefficient, in two large-scale proteomics datasets (Kustatscher et al., 2019; Lapek et al., 2017). Third, for each interacting protein pair, we computed the similarity of subcellular colocalization, again using the Pearson correlation coefficient to quantify similarity in two alternative subcellular proteomics datasets (Geladaki et al., 2019; Orre et al., 2019). The distribution of each metric within each network was visualized as a spectrum, using a random sample of 1,000 interacting protein pairs for the coexpression and co-localization spectra. Networks were arranged by the proportion of GO terms or proteins with less than random functional coherence (that is,  $AUC < 0.5$  or assortativity  $< 0$ ), coexpression, or colocalization (correlation  $< 0$ ).

### Literature-curated interactions

The master database of unique mouse interactions described above was used to define known interactions and identify interactome orphans as proteins in the mouse tissue interactomes for which no interactions were previously deposited in any interaction database (Kotlyar et al., 2015). The statistical significance of the overlap between the PCP-SILAM and literature-curated mouse interactomes was calculated using the hypergeometric test, defining the population size to be the total potential number of interactions between all unique proteins present in either the union of all PCP-SILAM tissue interactomes or the literature-curated dataset. Experimentally determined binding affinities of known protein-protein interactions were determined from the PDBbind database (Liu et al., 2015), after mapping human proteins to their mouse orthologs, and the binding affinities of interactions detected by PCP-SILAM were compared to the background of all affinities in the database. Proteins of unknown function were defined as proteins without any GO term annotation in the UniProt GOA database. To characterize functional differences in the PCP-SILAM and literature-curated interactomes, we adapted the approach of van Leeuwen et al. (2016). For each GO term or pair of GO terms in the GO slim, we computed the proportion of interactions between proteins annotated with the GO term(s) of interest in either the literature-curated interactome or the union of PCP-SILAM interactomes. We then computed the total possible number of interactions in either network, based on the total number of proteins annotated with the GO term(s) of interest in the network, and divided this by the total number of possible protein pairs to obtain the background proportion. We then used these proportions to calculate the enrichment for each network separately, and calculated the difference in enrichment between the literature-curated and PCP-SILAM interactomes as an odds ratio. Statistical significance was assessed via a Z test, with Benjamini-Hochberg correction. Markov clustering was performed on the union of the literature-curated and PCP-SILAM interactomes using the R package MCL, allowing self-loops and otherwise with default parameters. Each cluster was subsequently categorized based on whether the set of proteins therein was connected by literature-curated interactions only, PCP-SILAM interactions only, or both. To produce Figure 3G, the number of publications for each gene was calculated using the NCBI file gene2pubmed. Proteins were then divided into 40 evenly sized bins based on the number of publications in which they were mentioned, and the number of interactions between proteins in each pair of bins was calculated, following the methodology of Rolland et al. (2014). Protein abundance in mouse NIH 3T3 mouse fibroblasts was obtained from Schwanhäusser et al. (2011) and used to organize the mouse interactome by protein abundance following an analogous procedure.

### Predicted tissue interactomes

Predicted interactomes for six tissues, based on tissue-specific gene expression, were obtained from IID (Kotlyar et al., 2016); a predicted interactome was not available for thymus. Alternatively, predicted tissue interactomes were constructed in an analogous manner using protein or phosphoprotein expression data from Geiger et al. (2013) and Huttlin et al. (2010), respectively. Predicted tissue interactomes were constructed by subsetting the entire IID interactome to include interactions between proteins (phosphoproteins) expressed in that tissue. Mouse tissue-specific gene coexpression networks were constructed for six tissues; an insufficient number of samples were available for skeletal muscle. Curated microarray samples of healthy mouse tissues from the Affymetrix GeneChip Mouse Genome 430 2.0 platform were identified using Bgee (Bastian et al., 2021) and downloaded from ArrayExpress (Kolesnikov et al., 2015). Samples were processed using BrainArray Custom CDF (Dai et al., 2005) version 21.0.0 and normalized using MAS5 (Hubbell et al., 2002). Probes called as present in fewer than 20% of samples for each tissue were removed. ComBat (Leek et al., 2012) was used to adjust for batch effects, using each experiment as a batch, following best practices (Vandenberg et al., 2016). Finally, coexpression networks were constructed by taking the top 0.5% of connections, using the Pearson correlation as the similarity measure.

To quantify the enrichment for experimentally detected interactions in tissue-specific coexpression networks and predicted tissue interactomes, we compared the observed number of interactions overlapping between predicted and PCP-SILAM interactomes to the number of overlapping interactions when tissue interactomes were randomly rewired 100 times using a degree-preserving algorithm (Maslov and Sneppen, 2002). The number of iterations for the edge rewiring algorithm was set to 6.9 times the number of edges in each network (Ray et al., 2012). Analysis of network topology was performed using the R package igraph (Csardi and Nepusz, 2006). Hub proteins were defined as the top 10% most connected proteins in each network (Batada et al., 2006). The overlap between hub proteins across tissues in both PCP-SILAM and predicted interactomes was quantified using the Jaccard index. The tendency for a protein to interact with different partners across tissues was quantified as the mean Jaccard index across all tissue pairs, with a lower Jaccard index reflecting greater rewiring of protein interactions and a higher Jaccard index reflecting relatively stable interactions across tissues. Enrichment or depletion for interactions at each level of specificity was calculated by calculating the ratio of interactions observed at each tissue specificity relative to random expectation, using the same rewired interactomes as above. No interactions were observed in five or more tissues within randomized networks.

### Evolutionary analysis of tissue interactomes

The evolutionary conservation of interactions detected by PCP-SILAM was evaluated by comparing interactions at each level of tissue-specificity (that is, interactions detected in one tissue, two tissues, three tissues, and so on) to (i) literature-curated interactions in model organisms, and (ii) systematic screens for protein-protein interactions in humans. Evolutionary conservation of mouse interactions in *Saccharomyces cerevisiae*, *Caenorhabditis elegans*, and *Drosophila melanogaster* was calculated using model organism-specific interactions from BioGRID (Oughtred et al., 2019). Mouse proteins were mapped to their one-to-one orthologs in each organism, as well as human, using InParanoid (Sonnhammer and Östlund, 2015). Human protein-protein interaction screens were obtained and preprocessed as described above. We also sought to evaluate the evolutionary novelty of tissue-specific interactions using unbiased, genome-wide datasets. To this end, the difference in evolutionary rates between interacting protein pairs was calculated as in Fraser et al. (2002), and phylogenetic profiles were constructed using the InParanoid database, with the similarity in phylogenetic profile of a protein pair defined as the Pearson correlation in the presence or absence of each protein across all species (Fortelny et al., 2017). Estimates of protein evolutionary age were obtained from ProteinHistorian (Capra et al., 2012). To ensure that significant correlations between tissue specificity and evolutionary conservation were not affected by higher false-positive rates for interactions detected in fewer tissues, we performed two additional sets of analyses. First, we removed all the interactions that were detected in only a single tissue and repeated all analyses using interactions found in anywhere from 2 to 7 tissues. Because these interactions were independently detected at least twice, they are highly unlikely to be false positives. Second, we calculated partial Kendall correlations, controlling for the precision at which each interaction was detected in each tissue. We found the results remained statistically significant in all cases (Table S6).

To analyze cross-talk between tissue-specific and housekeeping proteins, we calculated the tissue specificity of each individual protein as the number of tissues in which it was quantified in at least one PCP-SILAM fraction. We then calculated the statistical significance of the over- or under-representation of interactions between housekeeping proteins and proteins detected in one to seven tissues based on the randomly rewired interactomes described above, as shown schematically in Figure S5D, and using Bonferroni correction to correct for multiple hypothesis testing. That is, we calculated the number of interactions in the liver interactome between proteins detected exclusively in the liver and proteins found in all seven tissues, in both real and randomly rewired networks, and expressed this as a Z score. We then repeated a similar calculation for proteins found in two to seven tissues in the liver interactome, and then repeated this entire procedure for the six remaining tissues. To assess statistical significance across all seven tissues, Z scores were aggregated using Stouffer's method, weighting each Z score by the number of interactions detected in that tissue.

### Interaction rewiring across tissues

We developed a quantitative index reflecting the degree of interaction rewiring for each protein across the seven mouse tissues in our study based on the Jaccard index of its interacting partners, as depicted schematically in Figure 6A. Briefly, for each of the 21 tissue pairs in turn, we computed the Jaccard index for each protein present in both networks, defined as the number of interactions present

in both tissues (the intersection) divided by the total number of interactions present in either tissue (the union). We then calculated the mean Jaccard index for each protein over all tissue pairs.

We then asked whether we could leverage this index to identify biochemical determinants of interaction rewiring. To this end, enrichment analysis of rewired proteins was performed using data from the following sources. Intrinsically disordered proteins were identified using IUPred (Dosztányi et al., 2005), with proteins containing more than 30% disordered residues categorized as intrinsically disordered (Gsponer et al., 2008). Proteins containing linear motifs were identified using ANCHOR (Mészáros et al., 2009). Protein phosphorylation data was obtained from Huttlin et al. (2010), and the tissue specificity of each phosphorylation site was quantified by calculating the Gini coefficient of the spectral counts in each tissue, a measure of inequality that has previously been used to quantify the tissue specificity of gene expression (O'Hagan et al., 2018). We tested for differences in the median Jaccard index across these categories using the Brunner-Munzel test, a nonparametric test of stochastic equality, as implemented in the R package 'lawstat.' The association between phosphorylation tissue specificity was tested using the Spearman rank correlation. Partial Spearman correlations, controlling for intrinsic disorder, were calculated using the 'ppcor' R package.

We then investigated whether interaction rewiring resulted in the formation of tissue-specific interactions involved in cell-cell signaling. We tested for associations between interaction tissue specificity and the presence of a protein kinase, transcription factor, or cell surface receptor using the Kendall rank correlation. Transcription factors were obtained from the Mouse TF Atlas (Zhou et al., 2017). Cell surface protein receptors were obtained from Ramilowski et al. (2015). Protein kinases were obtained from the UniProt protein kinase index (<https://www.uniprot.org/docs/pkinfam>). Edge betweenness centrality, a topological metric that reflects information flow through a network and is defined as the number of shortest paths between any two proteins that pass through a given edge, was calculated in the aggregate PCP-SILAM interactome formed by the union of unique interactions across all seven tissues, using the R package 'igraph' (Csardi and Nepusz, 2006).

We subsequently asked whether cellular strategies were in place to regulate the availability of rewired proteins. Protein and mRNA abundance, half-lives, and translation and transcription rates were obtained from Schwanhäusser et al. (2011). We then computed associations with the mean Jaccard index using the Spearman rank correlation, and again performed partial correlation analyses using the 'ppcor' R package. To evaluate the impact of technical limitations in the detection or quantification of low-abundance proteins on these findings, we performed two additional Jaccard index calculations. First, we reasoned that restricting our analysis to proteins that were detected in all seven tissues would mitigate the impact of sporadic protein identification. Accordingly, we filtered the tissue interactomes to include only interactions between these 'housekeeping' proteins, then repeated the Jaccard index calculation. Second, we divided the proteins identified in this study into three bins of lowly, moderately, and highly abundant proteins, based on their summed total intensity across all fractions. We then removed proteins from the bottom two bins from the tissue interactomes and repeated the Jaccard index calculation only for the top tercile of highly abundant proteins.

Last, we analyzed the relationship between interaction rewiring and disease. Mouse disease genes were obtained from the Mouse Genome Database (Smith et al., 2018). Tissue-specific disease genes, and their associated tissues, were obtained from Basha et al. (2020), and network interconnectivity was calculated using the mean shortest path as previously described (Menche et al., 2015b), restricting the analysis to disease-tissue pairs in which at least four disease genes were present in the corresponding tissue interactome. The Brunner-Munzel test was used to evaluate the difference in network interconnectivity between disease-associated and non-disease-associated tissues.

# Supplemental figures

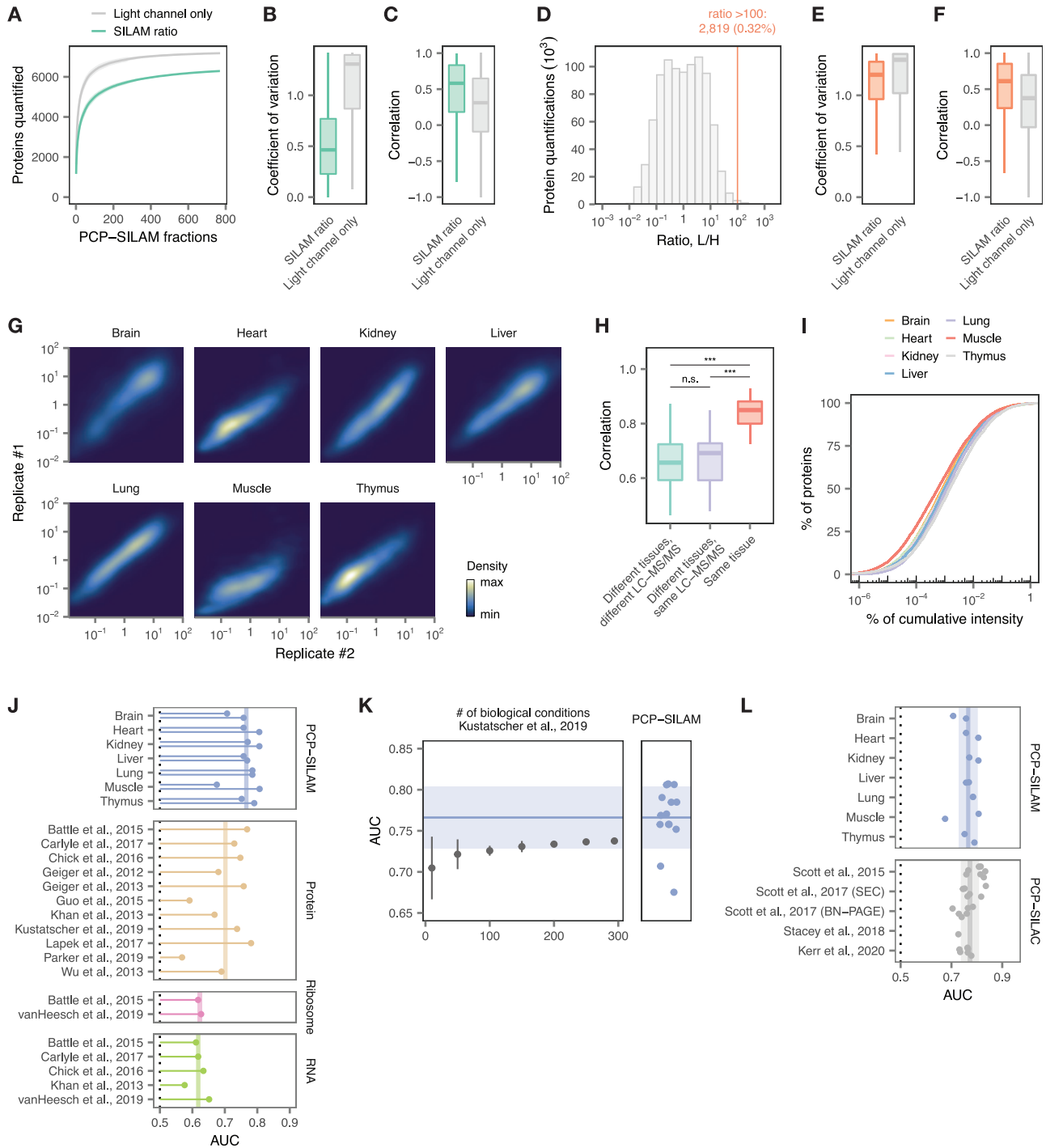


**Figure S1. Quantitative profiling of mouse tissue interactomes by PCP-SILAM, related to Figure 1**

(A) Saturation curve of unique proteins identified with random addition of PCP fractions, using either SILAM light/heavy ratios or the light channel only. The total number of protein groups quantified by SILAM is constrained by the requirement of quantification in both the unlabelled sample and the SILAM global reference. The mean and standard deviation of 100 bootstraps are shown.

(legend continued on next page)

- 
- (B) Coefficient of variation (CV) between biological replicates for individual protein quantifications, using either SILAM light/heavy ratios or the light channel only for protein quantification.
- (C) Rank correlation between biological replicates for entire protein chromatograms, using either SILAM light/heavy ratios or the light channel only for protein quantification.
- (D) Distribution of SILAM ratios across all tissues and replicates. Orange line and text show the number of proteins in the dataset with SILAM ratios greater than 100.
- (E) Coefficient of variation (CV) between biological replicates for individual protein quantifications, using either SILAM light/heavy ratios or the light channel only for protein quantification, including only individual quantifications with SILAM ratios greater than 100.
- (F) Rank correlation between biological replicates for entire protein chromatograms, using either SILAM light/heavy ratios or the light channel only for protein quantification, including only chromatograms containing at least one SILAM ratio greater than 100.
- (G) Reproducibility of PCP-SILAM protein quantification within individual tissues.
- (H) Rank correlations between pairs of mismatched tissues acquired using either the same or different LC-MS/MS setups, or between matching tissue pairs. n.s.,  $p = 0.47$ , Wilcoxon rank-sum test; \*\*\* $p < 0.0001$ , Wilcoxon rank-sum test.
- (I) Cumulative distribution of protein intensity across tissues, shown as a fraction of measured total protein intensity within each tissue.
- (J) Recovery of known protein complexes based on co-abundance in PCP-SILAM fractions or large-scale proteomic, transcriptomic, or translatic datasets, for each individual dataset shown in [Figure 1G](#).
- (K) Recovery of known protein complexes based on co-abundance in PCP-SILAM or coexpression in subsets of between 10 and 300 experiments from the ProteomeHD resource.
- (L) Recovery of known protein complexes in PCP-SILAM and published, cell-line-based PCP-SILAC datasets.

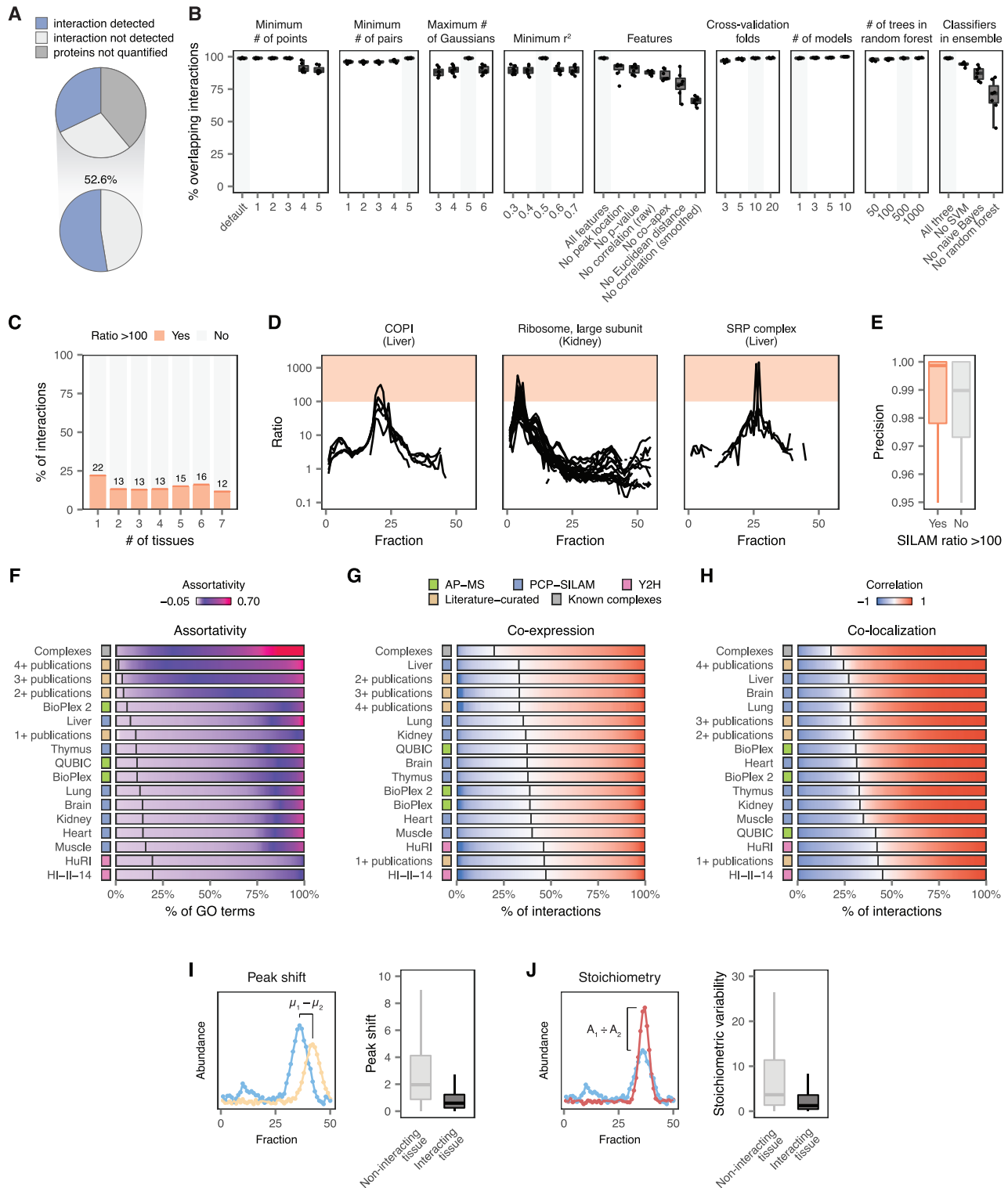


**Figure S2. Validation of mouse tissue interactomes, related to Figure 2**

(A) Proportion of intra-complex interactions detected within the training set of known protein complexes amenable to analysis by PCP.

(B) Proportion of interactions recovered within each tissue interactome when varying the parameters used by PrInCE for network inference. Light gray bars indicate the default parameters.

(C) Proportion of unique interactions detected in between one and seven tissues involving a protein with a SILAM ratio greater than 100 in at least one tissue.

(legend continued on next page)

---

(D) Examples of well-characterized protein complexes with SILAM ratios greater than 100 in at least one tissue.

(E) Minimum precision at which interactions involving proteins with SILAM ratios greater than 100 were detected, compared to all other interactions.

(F) Assortativity of GO terms in interactome networks. Each vertical band represents a single GO term, shaded by its assortativity (that is, the tendency for proteins annotated with that GO term to be connected to other proteins annotated to the same GO term) in each interactome. Vertical lines indicate the proportion of GO terms with assortativity less than 0.

(G) Coexpression of interacting protein pairs in the ProteomeHD resource. Each vertical band represents one of 1,000 randomly selected interacting protein pairs, shaded by the Spearman correlation between the log-fold change ratios of the two interacting proteins across 294 SILAC proteomics experiments. Vertical lines indicate the proportion of negatively correlated interacting pairs.

(H) Co-localization of interacting protein pairs, as quantified by their correlation across cellular fractions in subcellular proteomics data (Orre et al., 2019). Each vertical band represents one of 1,000 randomly selected interacting protein pairs, shaded by the Spearman correlation between the abundances of the two interacting proteins across subcellular fractions. Vertical lines indicate the proportion of negatively correlated interacting pairs.

(I) Left, schematic depicting calculation of the peak shift. Right, peak shifts of interacting protein pairs in tissues where the interaction did or did not take place, as inferred by PrInCE.

(J) Left, schematic depicting calculation of the interaction stoichiometry. Right, standard deviation of the interaction stoichiometry across tissues where the interaction did or did not take place, as inferred by PrInCE.

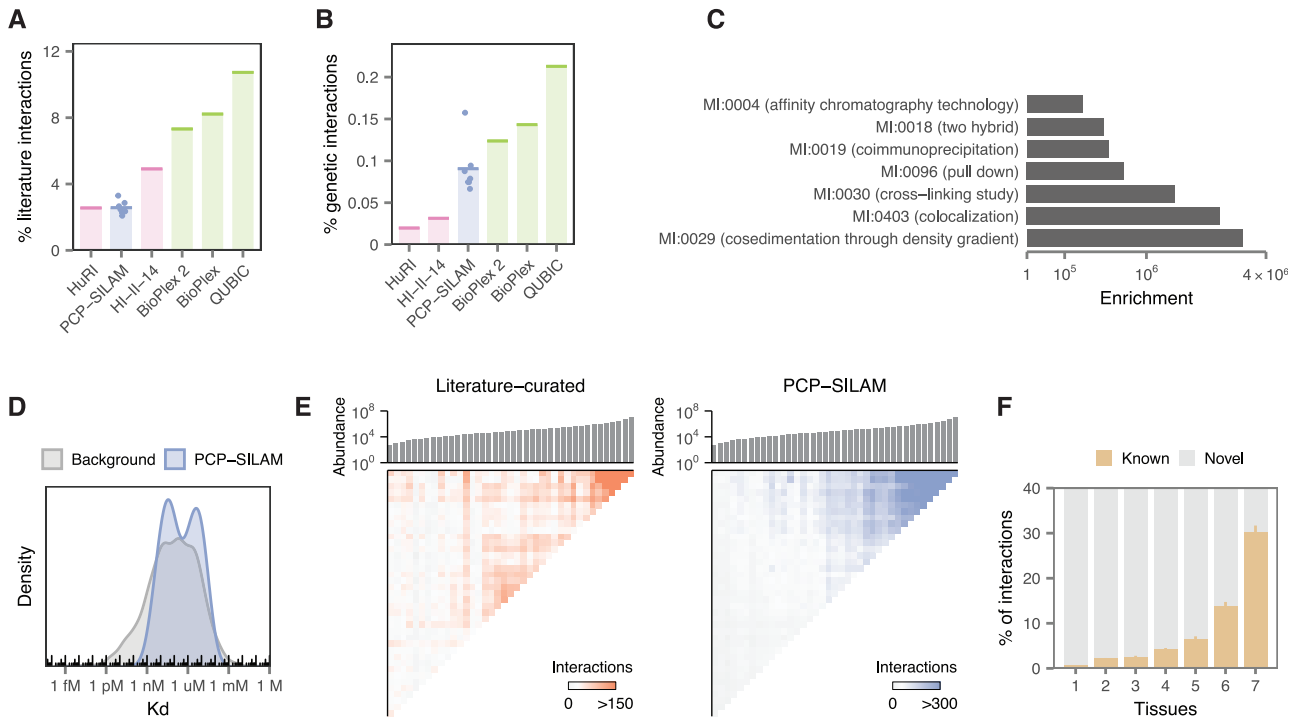
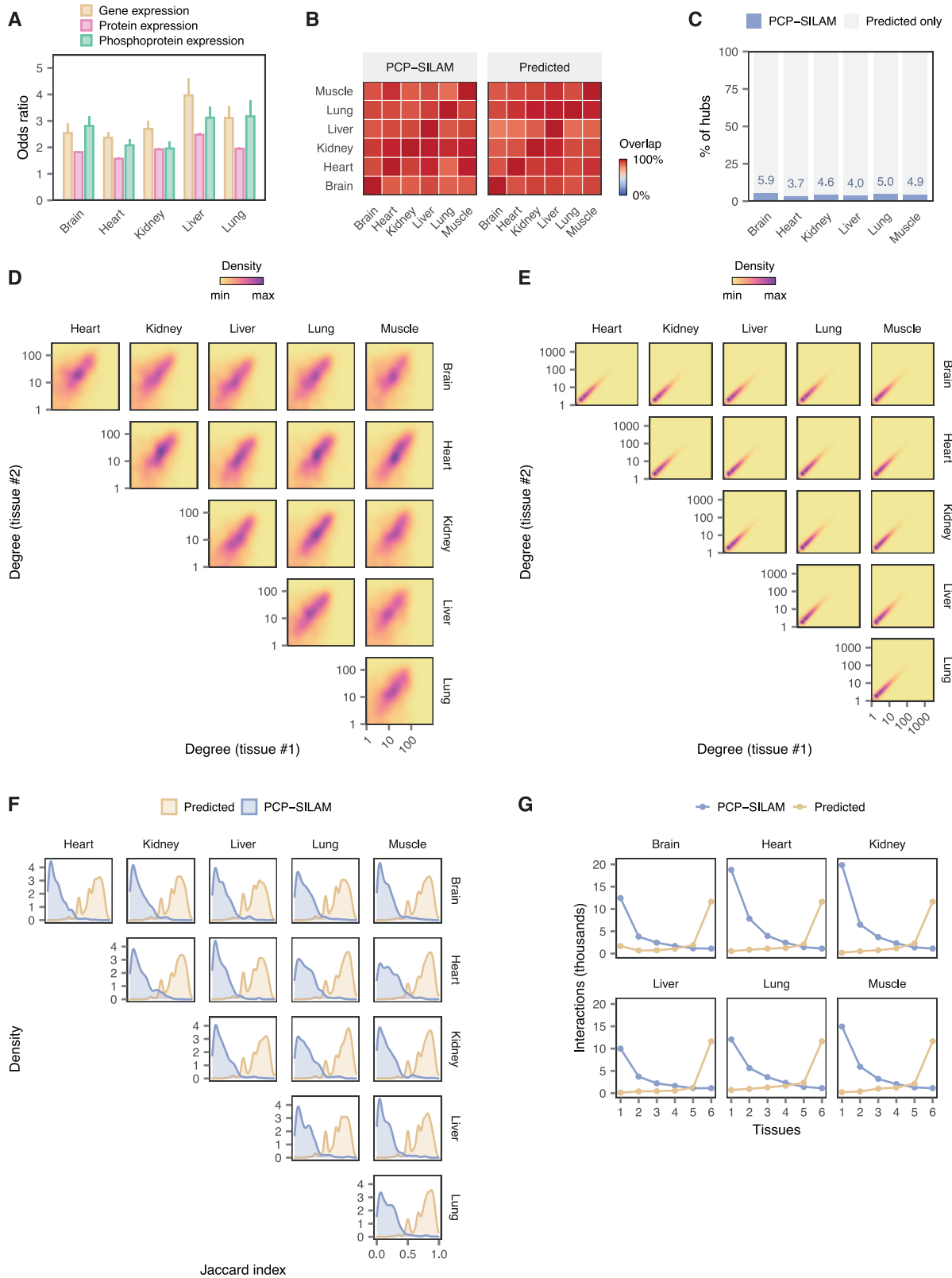


**Figure S3. Expansion of the known mouse interactome by PCP-SILAM, related to Figure 3**

- (A) Proportion of interactions detected here by PCP-SILAM and in five recent high-throughput human screens that overlap with a literature-curated human interaction. For PCP-SILAM, points show individual tissues and the bar shows the mean across tissues.
- (B) As in (A), but showing the proportion of interactions that overlap with a human genetic interaction.
- (C) Enrichment for overlap with literature-curated mouse interactions detected with different methods, relative to random expectation.
- (D) Experimentally determined binding affinities of protein-protein interactions in the PDBbind database and the subset of PDBbind recovered by PCP-SILAM.
- (E) Number of interactions between proteins binned by mean abundance (copies per cell) in mouse fibroblasts and ordered along both axes. Histogram shows the median abundance in each bin.
- (F) Proportion of previously known mouse interactions among PCP-SILAM interactions detected in one to seven tissues.



(legend on next page)

---

**Figure S4. Interactome rewiring limits accuracy of tissue interactome prediction, related to [Figure 4](#)**

- (A) Overlap between PCP-SILAM mouse tissue interactomes and tissue interactomes predicted by overlaying gene, protein, or phosphoprotein expression data onto a static interactome map, relative to rewired networks.
- (B) Proportion of hub proteins in one tissue (x axis) that are present in the interactome of the second tissue (y axis). Compare to [Figure 4C](#).
- (C) Most PCP-SILAM tissue interactome hubs are not hubs in the corresponding predicted tissue interactomes.
- (D-E) Protein degrees across tissues in PCP-SILAM (D) and predicted (E) tissue interactomes.
- (F) Rewiring of protein interaction partners across each pair of tissues, as quantified by the Jaccard index, in predicted and PCP-SILAM tissue interactomes.
- (G) Tissue specificity of interactions across predicted and PCP-SILAM tissue interactomes.

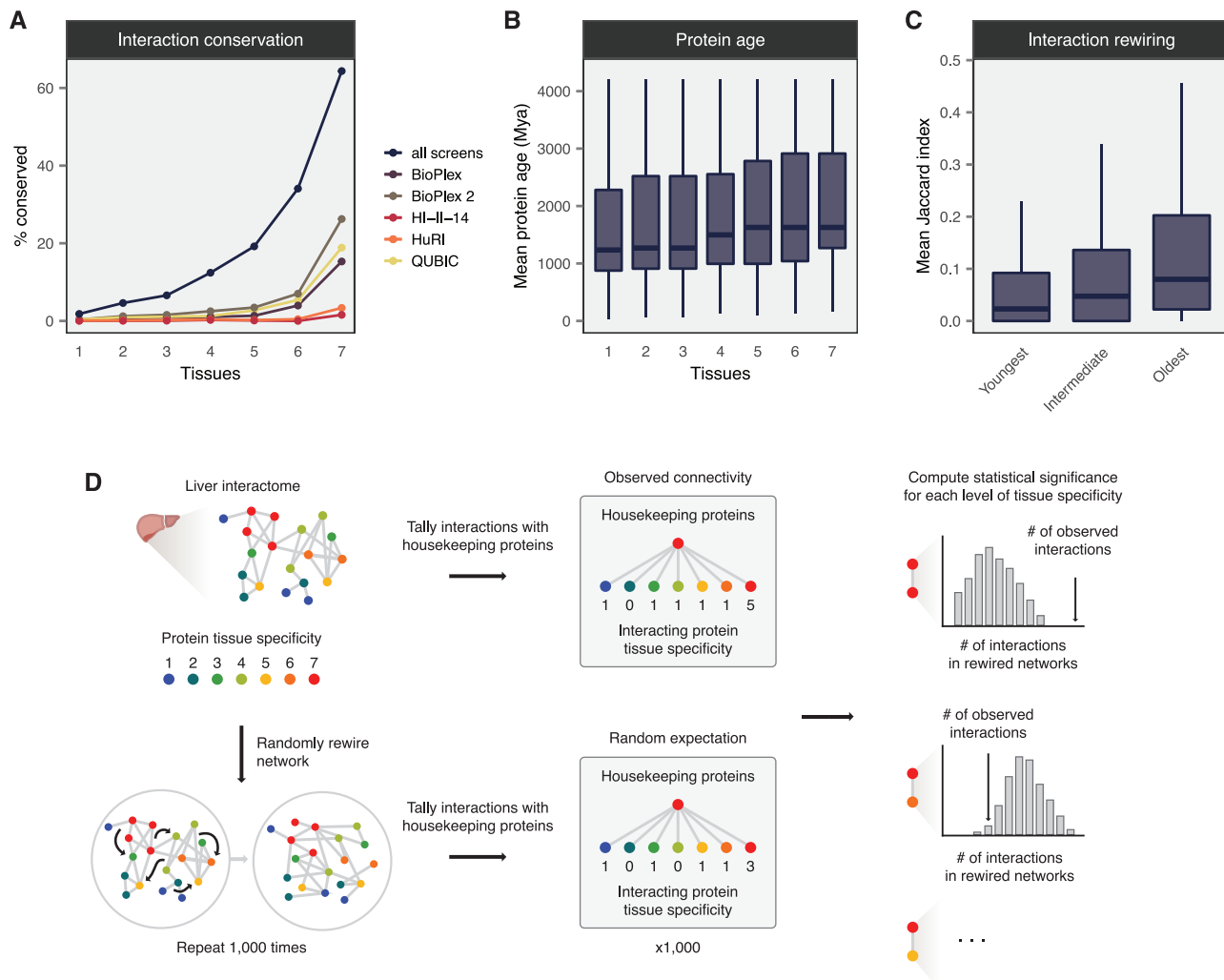


**Figure S5. Evolution of interactions in mouse tissues, related to Figure 5**

(A) Proportion of mouse interactions conserved in human, at each level of tissue specificity, in five recent high-throughput human interactome screens.

(B) Mean evolutionary age of interacting protein pairs at each level of tissue specificity.

(C) Mean Jaccard index across all pairs of tissue interactomes for mouse proteins binned by evolutionary age.

(D) Illustration of the randomized network null model. Within each tissue interactome, the observed number of interactions between housekeeping proteins (that is, proteins quantified in all seven tissues) and proteins quantified in between one and seven tissues is tallied. The network is then rewired 1,000 times using a degree-preserving method (Maslov and Sneppen, 2002), and the connectivity in randomly rewired networks is used to evaluate the statistical significance of the connectivity patterns in the observed tissue interactomes.

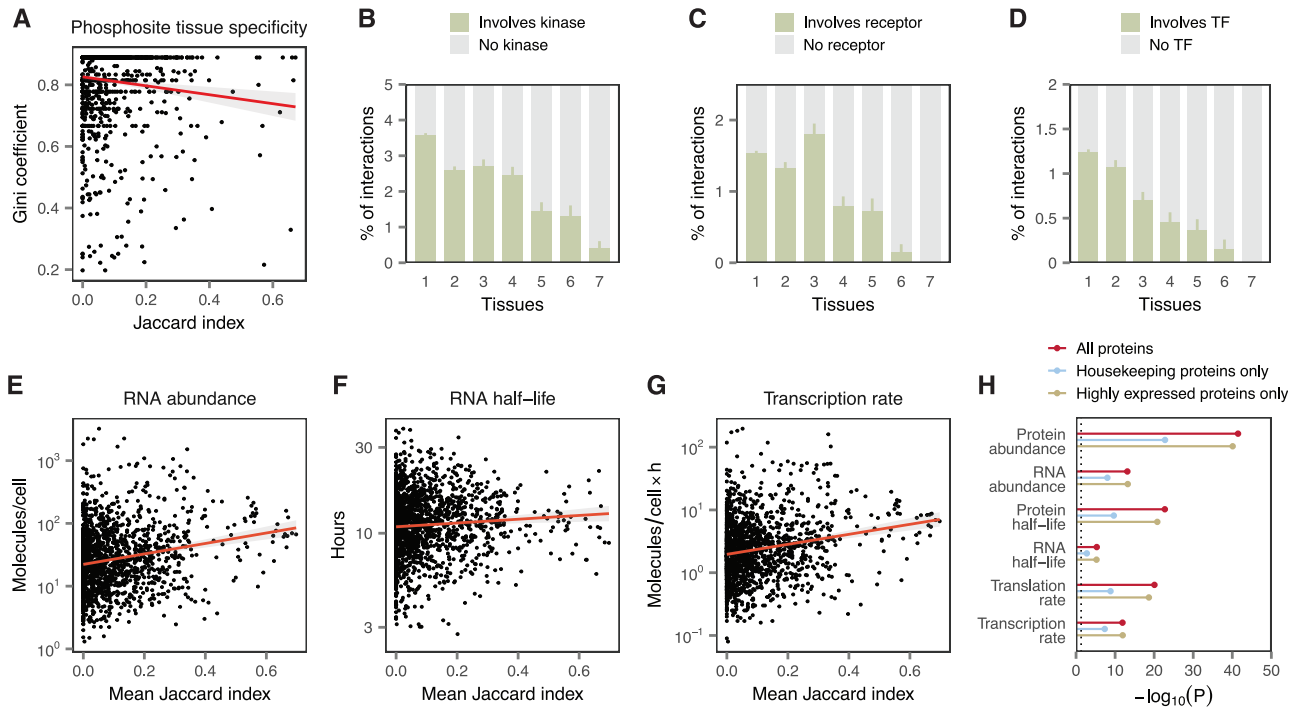


**Figure S6. Tissue-specific interactions mediate tissue-specific biological information flow, related to Figure 6**

(A) Phosphorylation sites on rewired proteins are more tissue-specific.

(B) Proportion of interactions involving protein kinases at each level of tissue specificity.

(C) Proportion of interactions involving transcription factors at each level of tissue specificity.

(D) Proportion of interactions involving cell surface receptors at each level of tissue specificity.

(E-G) mRNAs encoding rewired proteins are characterized by low abundance (E), short half-lives (F), and slow transcription rates (G).

(H) Statistical significance (Spearman rank correlation) of associations between the mean Jaccard index and protein and RNA abundances, half-lives, and transcription/translation rates when including only highly expressed proteins or proteins quantified in all seven tissues (housekeeping proteins) in the calculation of the Jaccard index. Dotted line shows  $p = 0.05$ .